Supporting Information

Computational Exploration of Adsorption-Based Hydrogen Storage in Mg-Alkoxide Functionalized Covalent-Organic Frameworks (COFs): Force-Field and Machine Learning Models

Yu Chen[1], Guobin Zhao[1], Sunghyun Yoon[1], Parsa Habibi[2], Chang Seop Hong[3], Song Li[4], Othonas A. Moultos[2], Poulumi Dey[5], Thijs J. H. Vlugt[2] and Yongchul G. Chung[1, *]

[1]*School of Chemical Engineering, Pusan National University, Busan 46241, Korea (South)*

[2]*Engineering Thermodynamics, Process & Energy Department, Faculty of Mechanical, Engineering, Delft University of Technology, Leeghwaterstraat 39, 2628 CB Delft, The Netherlands*

[3]*Department of Chemistry, Korea University, Seoul 02841, Republic of Korea*

[4]*Department of New Energy and Science Engineering, School of Energy and Power Engineering, Huazhong University of Science and Technology, Wuhan, 430074, China*

[5]*Materials Science and Engineering Department, Faculty of Mechanical, Engineering, Delft University of Technology, Merkelweg 2, 2628 CD Delft, The Netherlands*

**Corresponding author email: drygchung@gmail.com*

TABLE OF CONTENTS

S1. Recent studies on the ML prediction of H_2 adsorption on COFs 3

S2. Metrics used in this work.....4

S3. Version of Python packages used in this work.....5

S4. Electronic structure calculations and force field parameterization.....6

S5. Molecular models construction.....19

S6. High-throughput GCMC simulations of original and functionalized structures with specific FF models.....24

S7. Distribution of features and the H_2 adsorption uptakes of COFs in the dataset 34

S8. GCMC simulations of original and functionalized structures with specific FF models of two selected materials.....37

S9. Traditional tree-based ML models training.....42

S10. Crystal Graph Convolutional Neural Network (CGCNN) 48

S11. ML prediction of H_2 storage capacity of hypothetical COF structures in ReDD-COFFEE database (DB).....54

S1. Recent studies on the ML prediction of H_2 adsorption on COFs

Table S1. Recent studies on the ML prediction of H_2 adsorption on COFs

Year	Publication	ML model	Features	Target
2019	J. Phys. Chem. C[1]	Artificial Neural Network (ANN)	Structural properties, alchemical site number density, epsilon of H_2-alchemical sites, T and P conditions	H_2 loadings at various T and P
2020	J. Phys. Chem. C[2]	Ensemble Learning with Artificial Neural Networks (ANNs)	Canonical partition functions	Partition function of adsorbed fluids, then predict H_2 isotherm in COF-102
2023	J. Mater. Chem. A[3]	Tree-based Regressors	Structural and chemical properties	Adsorption and separation performance metrics for CH_4/H_2 mixtures

S2. Metrics used in this work

Coefficient of determination (R^2), mean absolute error (MAE), root-mean squared error (RMSE) was served as metrics in the optimization process of global optimization and machine learning models training. The definition of each metric can be represented as:

$$R^2 = 1 - \frac{\sum_{i=1}^{n}(y_i - \hat{y}_i)^2}{\sum_{i=1}^{n}(y_i - \bar{y})^2} \quad (1-1)$$

$$MAE = \frac{1}{n}\sum_{i=1}^{n}|y_i - \hat{y}_i| \quad (1-2)$$

$$RMSE = \sqrt{\frac{1}{n}\sum_{i=1}^{n}(y_i - \hat{y}_i)^2} \quad (1-3)$$

S3. Version of Python packages used in this work

Table S2. Version information of the Python packages used in this work

Package	Version
ase	3.22.1
mofun	1.0
numpy	1.26.4
pandas	2.2.1
pymatgen	2024.3.1
scikit-learn	1.5.2
scikit-optimize	0.10.2
scipy	1.10.1
shap	0.45.1
torch	2.2.2
xgboost	2.1.1

S4. Electronic structure calculations and force field parameterization

In this work, the interaction energies between H_2 and the Mg-alkoxide group were calculated at the MP2/6-311+G** level of theory with counterpoise corrections. These energies were estimated by subtracting the sum of the energies of each fragment from the counterpoise-corrected energy of the whole system, referred to as the "complexation energy (corrected)" in the Gaussian output file. For the MP2 calculation, default convergence criteria in Gaussian 16 Rev. C.01 software were used.

To simulate the scenario where one H_2 molecule approaching the Mg site from different directions and distances, six types of H_2-catecholate configurations were constructed, corresponding to the schematics shown in **Figure 2(b)**. The difference between type 1 and type 2 lies in the orientation of the hydrogen atoms relative to the phenyl ring. In type 1, both hydrogen atoms lie on the same plane as the phenyl ring. In type 2, however, the two hydrogen atoms are aligned along a bond that is perpendicular to the plane of the phenyl ring. This distinction is subtle but important in understanding the structural variation.

The geometry optimization results showed that the H_2 molecule did not dissociate into two hydrogen atoms, which would indicate chemisorption. The H-H bond length remained approximately 0.75 Å (75 pm), and the optimal distance between the H_2 center of mass and the Mg atom was around 2.2 Å, with a binding energy of approximately 20 kJ/mol. These findings confirm that the H_2 molecules are physiosorbed on the Mg sites, similar to other works in the field. For example, studies by Tsivion et al.[4], Veccham et al.[5], and Chakraborty et al.[6]

demonstrated that H_2 physisorption on metal-functionalized frameworks primarily involves weak van der Waals (vdW) interactions and polarization effects, without significant charge transfer or bond formation, which would indicate chemisorption.

To address the scenario where two H_2 molecules bind to both sites of a two-site functionalized structure, we also con-structed configurations with two H_2 molecules. These molecules were initially placed either on the same side or opposite sides of the catecholate. Followed by MP2 geometry optimization, binding energies were calculated using the same level of single-point calculations with counterpoise corrections. **Figure S1** shows the optimized configurations and corresponding average binding energies (overall binding energy divided by the number of H_2 molecules).

In the case (a) where only one H_2 molecule binds to one site of the functionalized catecholate, the binding energies for single-site and two-site functionalized catecholates are −21.59 kJ/mol and −19.70 kJ/mol, respectively. In case (b), where two H_2 molecules bind to the same site, the binding energies are −20.39 kJ/mol for the single-site and −18.06 kJ/mol for the two-site functionalized catecholates. In case (c), where two H_2 molecules bind to each site of the two-site functionalized catecholate, the average binding energy is −19.72 kJ/mol, which is 0.02 kJ/mol lower than one H_2 molecule adsorption on two-site functionalized catecholate. However, there is an appreciable difference in the binding energies when one H_2 molecule is adsorbed vs two H_2 molecule adsorbed on Mg sites (~1.5 kJ/mol). This difference in ad-sorption energy could lead to lower overall uptake for H_2. Unfortunately, we did not consider

the many-body affect in current work but future work should consider the impact of co-adsorbed H_2 as part of the force field development.

After calculating the interaction energies, the results were fitted to the force field (FF) models, as shown in **Schematics S1 to S3**, using the global optimization algorithm of dual annealing. This stochastic approach derived from the work by Xiang et al.[7] combines the generalization of Classical Simulated Annealing (CSA)[8] and Fast Simulated Annealing (FSA)[9] coupled to a strategy for applying a local search on accepted locations.[10]

During the FF fitting process, we considered only the Coulomb interactions between the H_2 adsorbates and the Mg, C, and O atoms in the Mg-alkoxide groups, assigning partial atomic charges only to these atoms and neglecting the others in the framework. To validate this assumption, we constructed single- and two-site functionalized moieties with three phenyl rings and performed MP2-level geometry optimizations and Natural Bond Orbital (NBO) analysis to obtain partial charge information. As shown in **Figure S2**, the partial charges on the Mg and O atoms in the functional groups are significantly larger than those on the other atoms. This supports the conclusion that concentrating the charge density primarily on the Mg-alkoxide groups for the functionalized structures is both reasonable and consistent with the available data.

Detailed parameters and settings can be found in **Tables S3 to S6**. Detailed results of the FF fitting are shown in **Figure S3 to S5**.

Schematic S1. Schematic of parameterization of the Modified-Morse force field model. Two different force field, namely FF1 and FF2, were obtained from the H_2 binding energies of single-site and two-site functionalized catecholates, respectively.

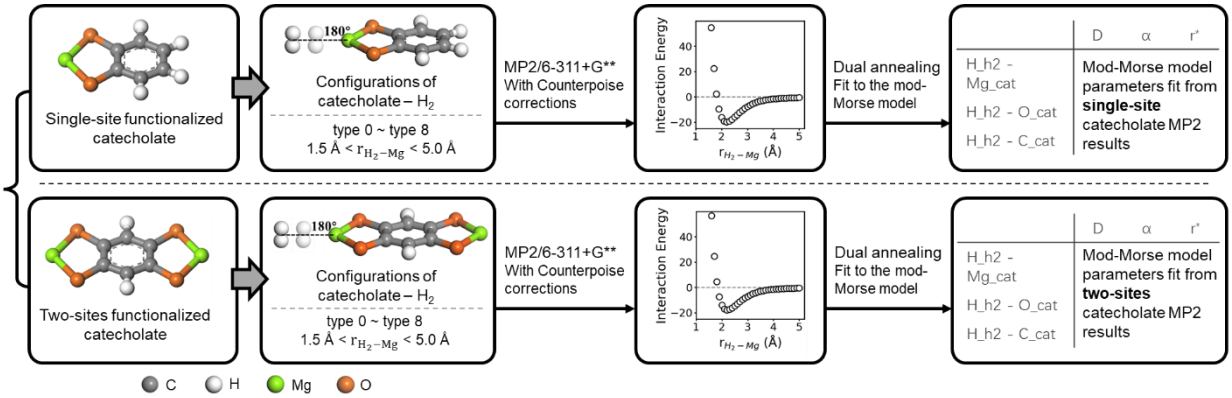

Schematic S2. Schematic of different potential models used for describing interatomic interactions (electrostatic interactions not included) between different atoms pairs. Modified-Morse potential was used to describe the interatomic interactions between H_2 and the atoms in the functional group, while the interatomic interactions between H_2 and other atoms were described by LJ potential model.

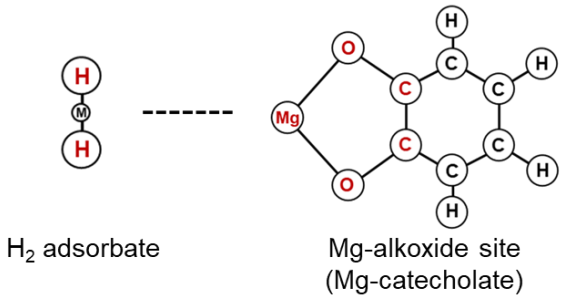

H_2 adsorbate Mg-alkoxide site (Mg-catecholate)

- for $H_{H_2} - Mg_{cat}$; $H_{H_2} - O_{cat}$; $H_{H_2} - C_{cat}$:

$$U_{modified-Morse}(r_{ij}) = -k_B D_{ij}\left[1 - \left(1 - e^{-\alpha_{ij}\left(r_{ij} - r_{ij}^{*}\right)}\right)^2\right]$$

- for H_{H_2} – other atoms in the catecholate :

$$U_{Lennard-Jones}(r_{ij}) = 4\varepsilon_{ij}\left[\left(\frac{r_{ij}}{\sigma_{ij}}\right)^{12} - \left(\frac{r_{ij}}{\sigma_{ij}}\right)^{6}\right]$$

Schematic S3. Schematic of finding the optimal sets of parameters by attempting to minimize the root-mean-square deviation (RMSE) between the interaction energies calculated from MP2 and FF models using global optimization method, in this work, dual annealing.

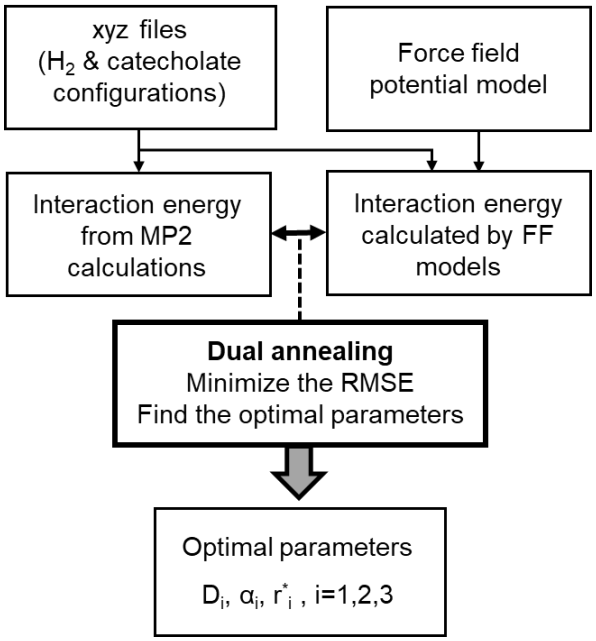

Table S3. Partial charges of the atoms of H_2 adsorbates and Mg-alkoxide functional groups

Atom	q
H_h2	0.468
H_com	−0.936
Mg_cat	1.25
O_cat	−0.625
C_cat	0.0

Table S4. Lennard-Jones force field parameters of framework atoms (outside the Mg-alkoxide functional sites) used in this work.

Atom Type	ε/k_b (K)	σ (Å)
B	47.81	3.58
Br	126.29	3.73
C	47.86	3.47
Cl	142.56	3.52
Co	7.04	2.56
Cu	2.52	3.11
F	36.48	3.09
H	7.65	2.85
N	38.95	3.26
Ni	7.55	2.52
O	48.16	3.03
S	173.11	3.59
Si	156	3.8
V	8.05	2.8
Zn	27.68	4.04

Table S5. Lennard-Jones force field parameters of the H_2 adsorbate atoms used in this work.

Atom Type	ε/k_b (K)	σ (Å)
H_h2	0.0	0.0
H_com	36.7	2.958

Table S6. Settings for dual annealing fitting

Setting	Parameter
Objective function	$RMSE(Energy_{inter,MP2}, Energy_{inter,FF})$
Bounds	D∈[1.0,1000.0], α∈[0.01,5.0], r*∈[0.1,10.0]
Maximum iteration	1000
Other parameters	Default values in *scipy.optimize.dual_annealing*

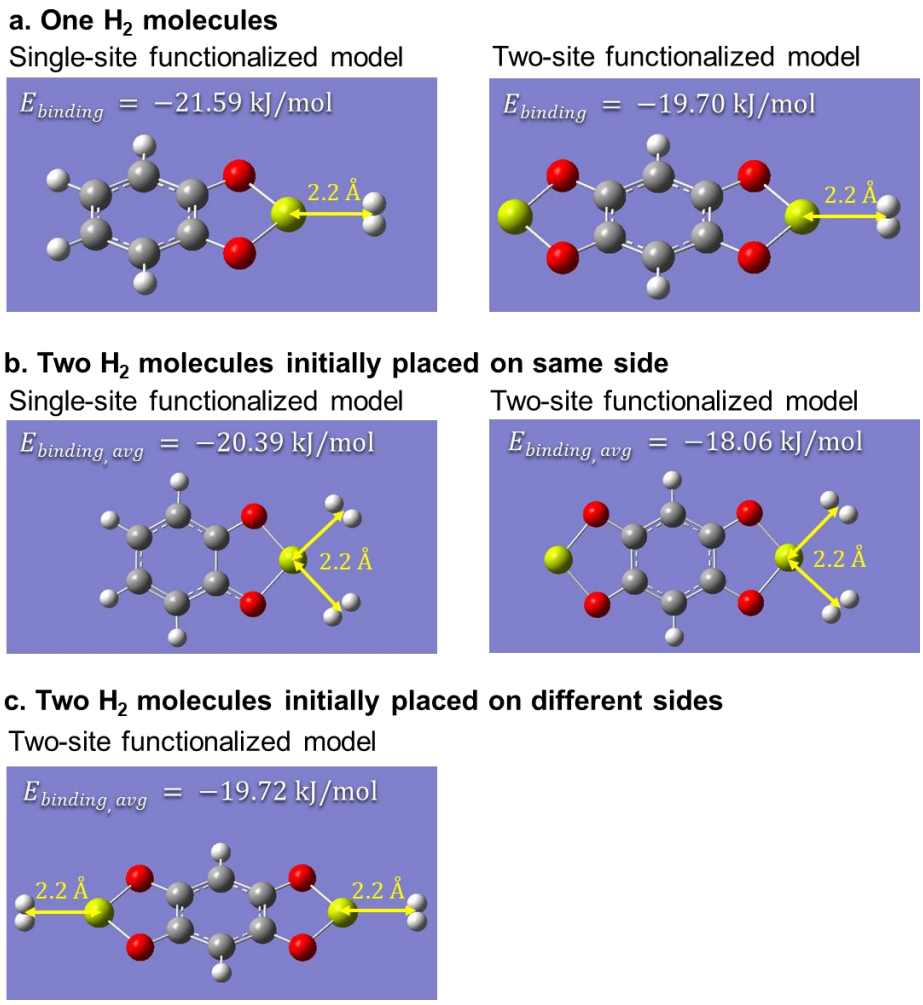

Figure S1. Average H_2 binding energies of different H_2-catecholate configurations.

a. Single-site functionalized

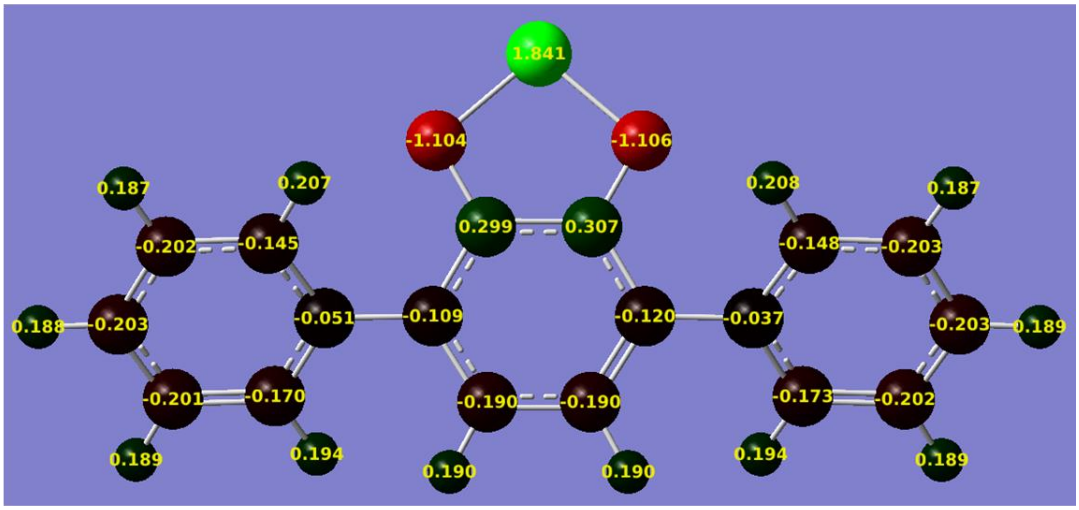

b. Two-site functionalized

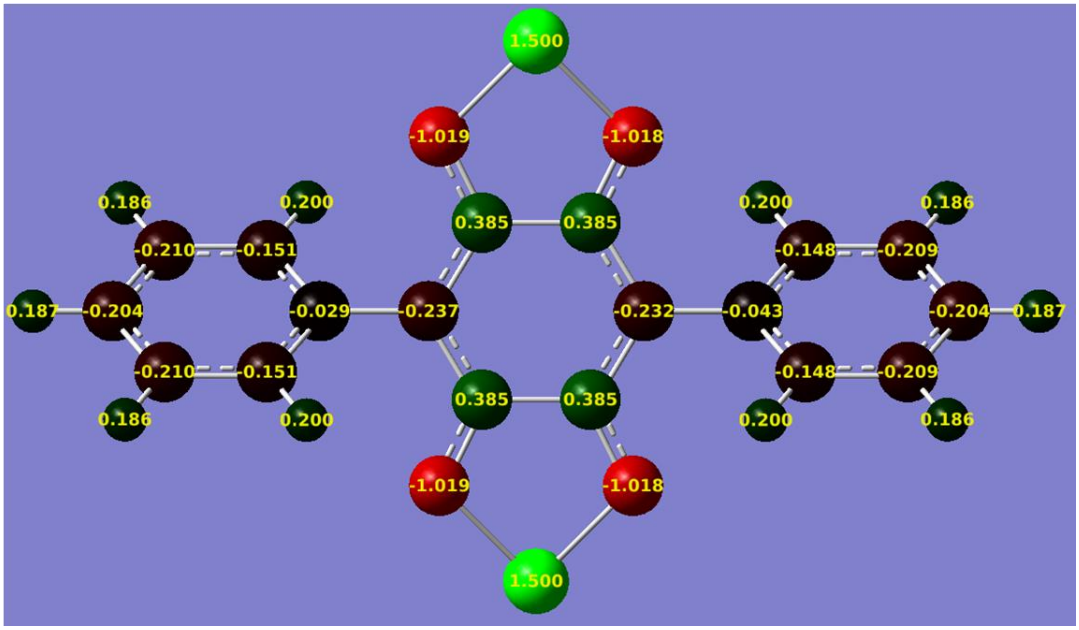

Figure S2. Partial atomic charges obtained from NBO analysis of the Mg-alkoxide functionalized moieties with three phenyl rings.

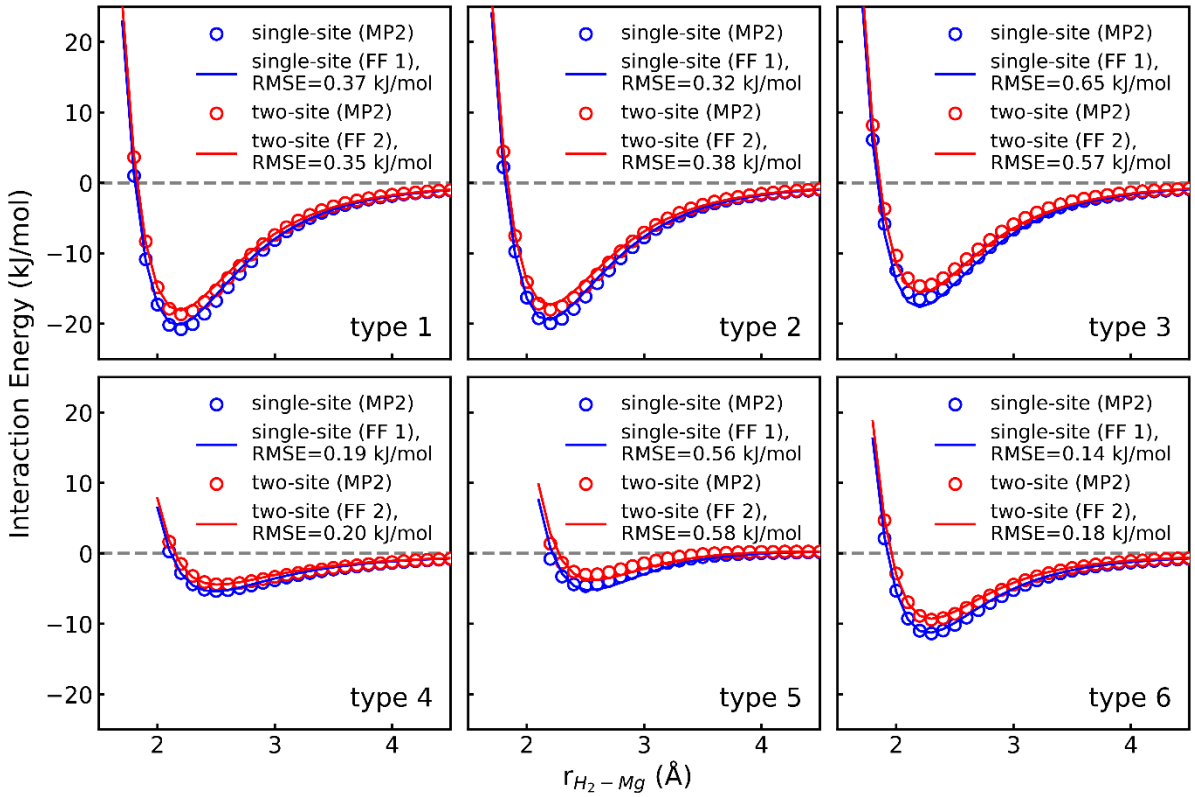

Figure S3. Detailed results of the FF fitting results. H_2 interaction energies calculated with the FF models (lines) compared with energies calculated by MP2 (circles). The RMSE values for each type of configuration and different FF models are shown in the legend.

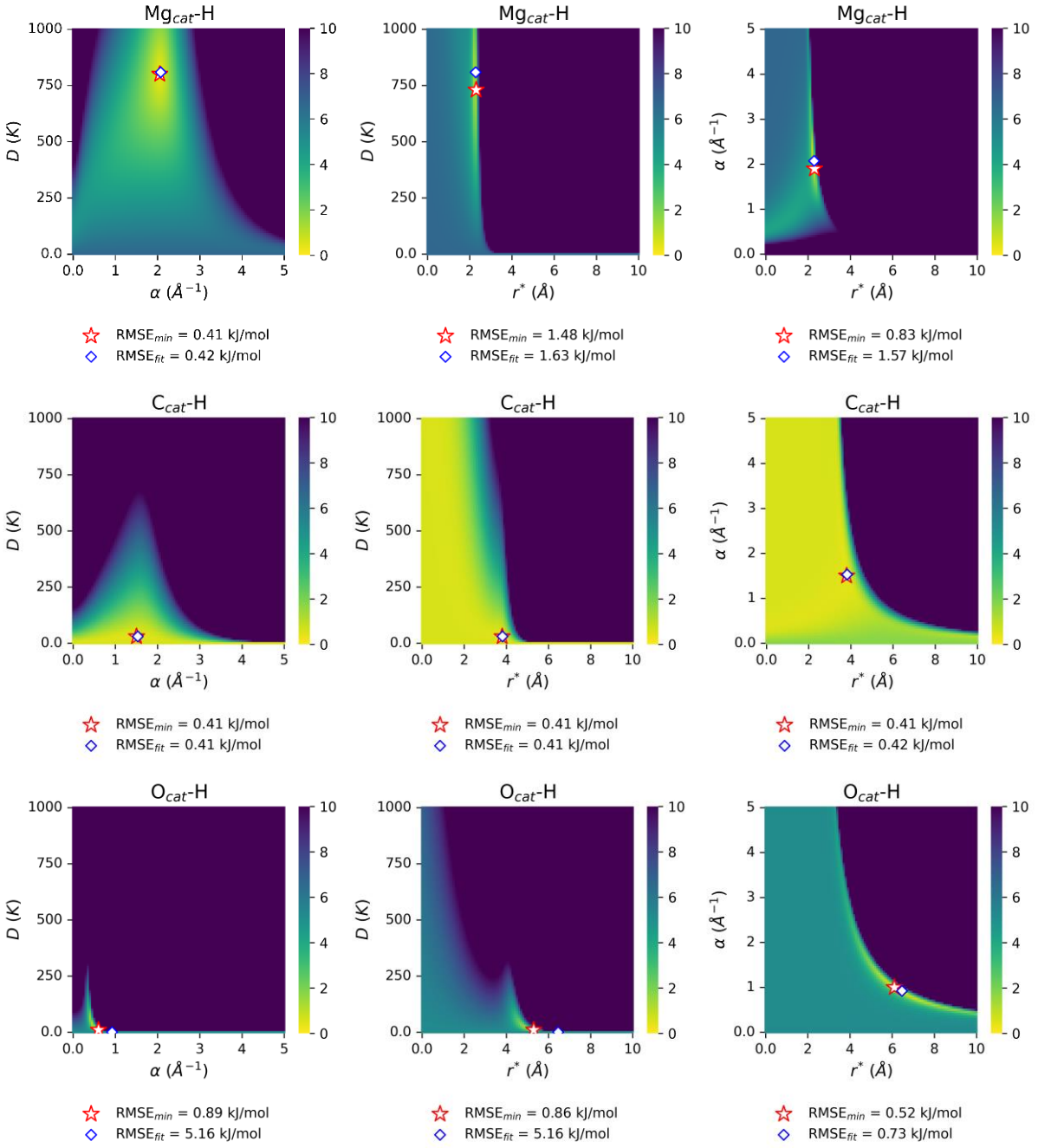

Figure S4. Sensitivity analysis of the **FF1** parameters. The color refers to the RMSE values between the binding energies calculated by the current set of parameters and those from MP2 calculations. The red stars represent the local minimum point and the blue squares represent the resulting optimal sets of parameters from global optimization.

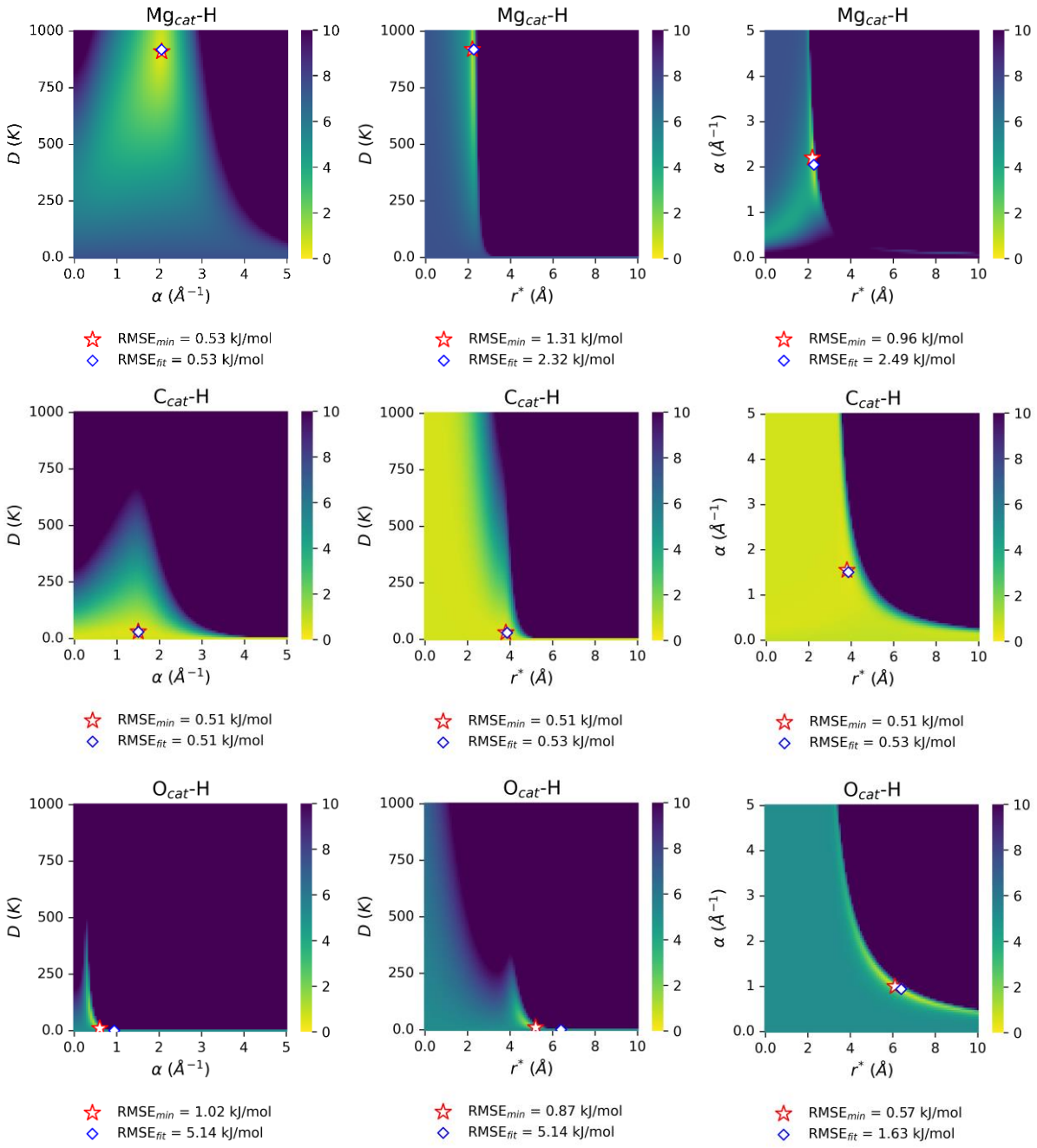

Figure S5. Sensitivity analysis of the **FF2** parameters. The color refers to the RMSE values between the binding energies calculated by the current set of parameters and those from MP2 calculations. The red stars represent the local minimum point and the blue squares represent the resulting optimal sets of parameters from global optimization.

S5. Molecular models construction

To implement the different types of functionalization with Mg-alkoxide groups, python package MOFUN and Julia package PoreMatMod were used for the definition of moieties, searching for replace sites, and replacement of the original queries with functionalized ones. Although the specific functions implementing these steps are different for these two packages, the workflows are the same. In the current workflow to generate functionalized COF structures, we used MOFUN program to detect and place alkoxide functional groups. For MOFUN, the process involved the following steps: first, the original and functionalized phenyl ring moieties for search and re-placement were loaded using the Atoms.load function. Next, the find_pattern_in_structure function was employed to identify all potential sites for functionalization, i.e., phenyl rings, within the structure. Finally, the re-place_pattern_in_structure function was used to replace the original phenyl rings with one- or two-site Mg-alkoxide functionalized ones, based on a defined replacement ratio (e.g., 50% or 100%). A tolerance value can be set to avoid the atomic overlapping after the replacement.

After modification, the Mg, O, and C atoms in the functional groups of the framework structures were labelled specifically to make sure the specific FF models are implement on these atoms. We implemented specialized force field models by modifying the CIF files with labeling the O and C atoms in the Mg-alkoxide groups as Te and Sn, respectively. For instance, in the CIF file, we changed the _atom_site_label from O12 to Te12 (or C13 to Sn13), while keeping the _atom_site_type_symbol unchanged as O (or C). In the RASPA2 input definition

files, we defined the force field parameters for these pseudo-atoms ("Te" and "Sn") using the Morse potential parameters for O_cat and C_cat atoms (_cat stands for the atoms in Mg-alkoxide group, as labeled in Table 1 in the manuscript), along with the corresponding mass and partial charge information.

There is no overall geometry optimization on the structures after the modification. The geometries of the single- and two-site functionalized phenyl rings used as the replacement moieties were from the MP2-optimized functionalized catecholate. The local structure around the functional groups can be considered as realistic after their integration into the larger COF structures, even without further overall geometry optimization.

To further investigate the importance of overall geometry optimization, we conducted rough geometry optimizations on two representative structures with 100% two-site functionalization: 21320N2 and 07010N3. These structures represent two typical classes of COFs -- one with larger pores and fewer functionalization sites, and another with smaller pores and more functional sites. The 100% two-site functionalization introduces the highest density of Mg-alkoxide sites, potentially leading to the most significant changes post-optimization.

We conducted geometry optimizations using DFT+D3 (PBE) with VASP 6.4.2, which converged after approximately 80 optimization steps. We observed that the Mg atoms moved away from the O atoms, and the alkoxide site functional group becomes distorted. The visualizations of an example structure, the 100% two-site functionalized structure 07010N3_two_all, before/after overall geometry optimization are shown in **Figure S6**.

We proceeded to compare the H_2 adsorption performance of the structures before/after DFT optimization using GCMC simulations under the same conditions as described in the manuscript. The H_2 adsorption isotherms with/without overall geometry optimization (DFT) are shown in **Figure S7**. The results demonstrated that the discrepancies in H_2 uptake between the optimized and non-optimized structures are minimal, with the absolute errors falling within an acceptable range.

In conclusion, for high-throughput screening in this work, the overall geometry optimization may not be necessary, as it adds considerable computational cost without significantly improving the accuracy of the adsorption predictions. For materials identified as top performers during the screening, we recommend conducting geometry optimization to obtain more precise adsorption performance data. Additionally, to prevent the distortion of Mg-alkoxide sites during optimization, adding water solvent molecules may stabilize the structure. However, this is beyond the scope of the current study and could be explored in future work.

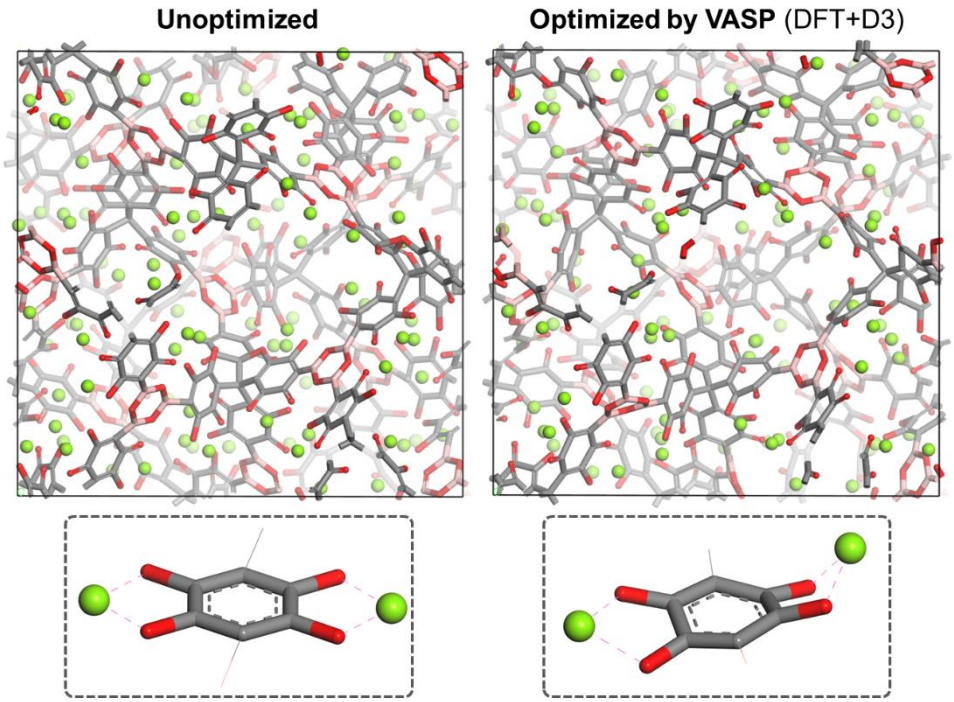

Figure S6. Visualization of the 100% two-site functionalized structure 07010N3_two_all: without overall optimization, and after optimization with VASP. The upper figures display the overall structures, while the lower figures highlight the moieties with Mg-alkoxide groups.

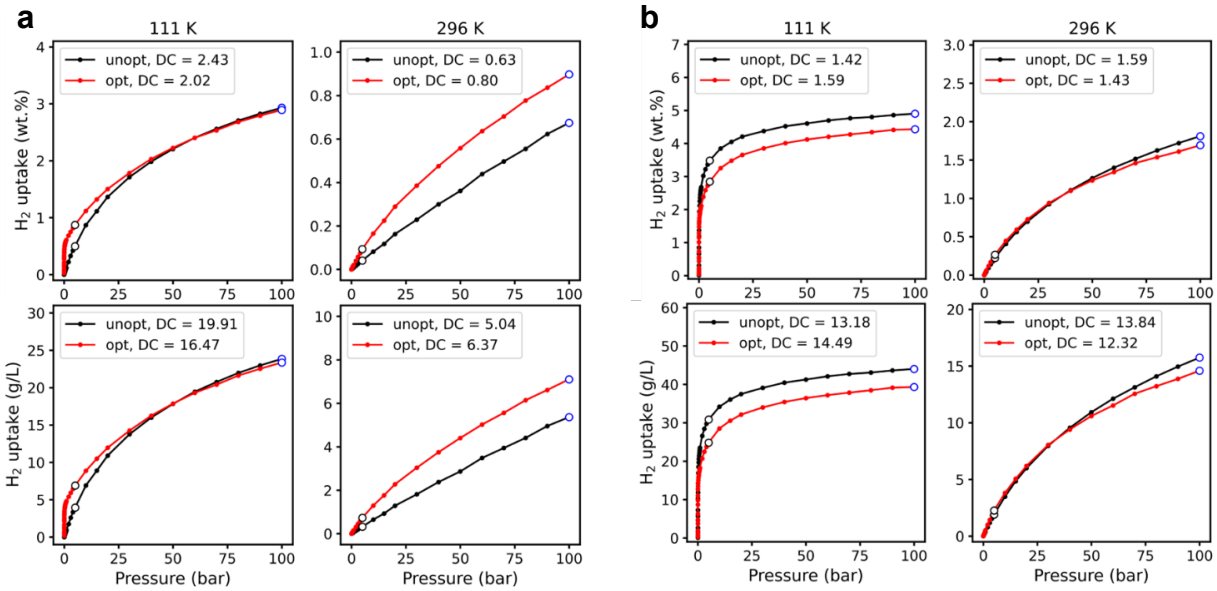

Figure S7. Comparison between the H_2 isotherms of the 100% two-site functionalized **(a)** 21320N2 and **(b)** 07010N3 with/without overall geometry optimization by DFT.

S6. High-throughput GCMC simulations of original and functionalized structures with specific FF models

Table S7 shows the DOE Technical Targets for Onboard Hydrogen Storage for Light-Duty Vehicles from the Hydrogen and Fuel Cell Technologies Office, used as our target of high-throughput screening.

Figure S8 shows the detail of the H_2 uptakes at different pressure points, corresponding to discussion in Section 3.2.1 and **Figure 3** in the main text.

Figure S9 shows the enhancement of the gravimetric and volumetric H_2 DCs after different types and ratios of functionalization, compared to the density of the original (unfunctionalized) structures.

To investigate the impact of framework charges on H_2 adsorption performance in original and functionalized structures, we performed GCMC simulations on the structures with and without partial atomic charges on the framework atoms. For the original unfunctionalized structure, the partial atomic charges information was estimated by DDEC6 and provided by the CURATED-COF database. For the Mg-alkoxide functionalized structures, we first predicted the charges of all framework atoms using the ML-based partial atomic charge estimation method PACMAN[11], then after fixing the atomic charges of Mg_cat, O_cat, and C_cat atoms at the functional sites as 1.250, -0.625, and 0.000, respectively. The net charge of the framework at this point was calculated. Then, the partial atomic charges of the framework

atoms outside the functional sites were adjusted by subtracting the net charge divided by the number of framework atoms outside the functional sites, to neutralize the overall charge of the framework. The distribution of partial atomic charges for each element in the original unfunctionalized structures (estimated by DDEC6) and the functionalized structures (modified from PACMAN-predicted results) is shown in **Figure S10**. The com-parison indicates that the distribution of framework charges outside the functional groups in the functionalized structures is similar to the DDEC6-estimated charges in the original unfunctionalized structures.

GCMC simulations for the 608 original structures without framework charge have been completed, while simulations for approximately 900 out of 1,843 functionalized structures with full framework charges have been finished. We have collected the results so far, and the exact number of data points for each plot is provided in the figure captions. **Figure S11** compares the H_2 DCs of original unfunctionalized structures with framework charges neglected or involved. The results show no significant difference between the DCs calculated with or without framework charges involved. Similarly, **Figure S12** compares the H_2 DCs of Mg-alkoxide functionalized structures with the charges outside functional sites neglected or involved. While there is some minor discrepancy, the overall results show no significant difference.

We also compared the percentages of van der Waals (vdW) and electrostatic energies from the total energies obtained during GCMC simulations of both original and several functionalized structures. **Figure S13** shows the proportions of vdW and electrostatic energies

in the total adsorbate-host energies after assigning framework charges to the original structures. For all 3,648 GCMC simulations of the 608 original structures, the electrostatic interactions energies were less than 5% of the total energies. In these cases, vdW energies dominated, and assigning framework charges (i.e., including host-adsorbate Coulomb energies) did not significantly impact the overall simulation results.

For the functionalized structures, assigning partial atomic charges only to the Mg and O atoms in the functional sites resulted in electrostatic interactions energies accounting for 30–40% of the total adsorbate-host energies during GCMC simulations. Assigning partial atomic charges to other framework atoms outside the functional sites did not significantly change the percentage of electrostatic interactions energies, with only minor differences observed, regardless of the functionalization type and ratio.

Based on the results, the interaction between H_2 adsorbates and the frameworks in the original structures is primarily driven by vdW forces, and neglecting framework charges (and thus host-adsorbate electrostatic interactions) does not significantly affect the simulated H_2 adsorption uptakes. For Mg-functionalized structures, electrostatic interaction energies contribute 30–40% of the total adsorbate-host energies, but this contribution remains unchanged whether or not partial charges are assigned to atoms outside the functional sites. As a result, it is reasonable to only consider the atomic charges on the Mg_cat and O_cat atoms at the functional sites in the functionalized structures during GCMC simulations.

Table S7. DOE Technical Targets for Onboard Hydrogen Storage for Light-Duty Vehicles

Storage parameter	**Unit**	**2020 target**	**2025 target**	**Ultimate target**
Usable, specific-energy from H_2 (net useful energy/max system mass)	wt.%	4.5	5.5	6.5
Usable energy density from H_2 (net useful energy/max system volume)	g/L	30	40	50

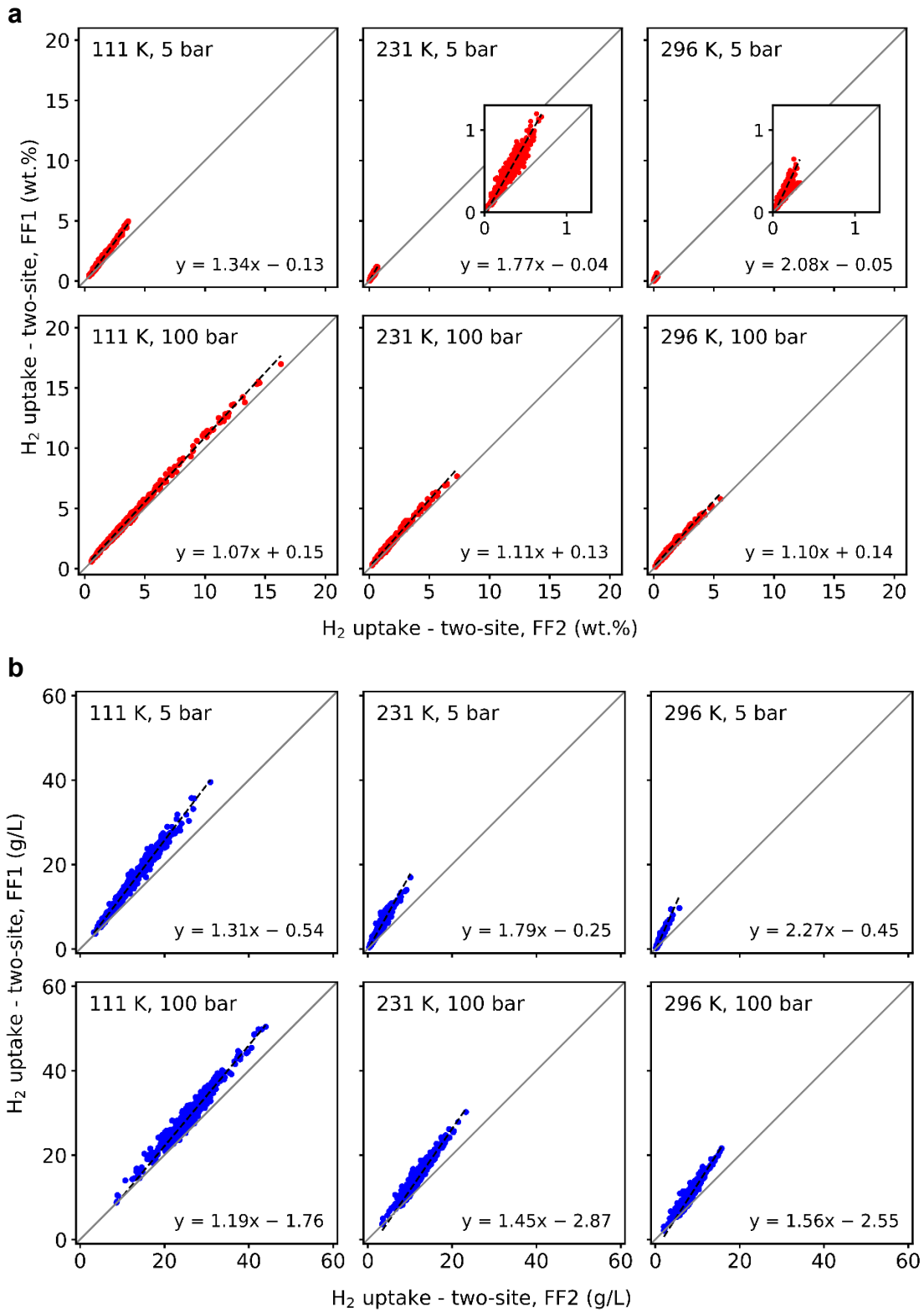

Figure S8. Comparison of the **(a)** gravimetric and **(b)** volumetric hydrogen uptakes of two-site functionalized structures calculated using FF1 and FF2.

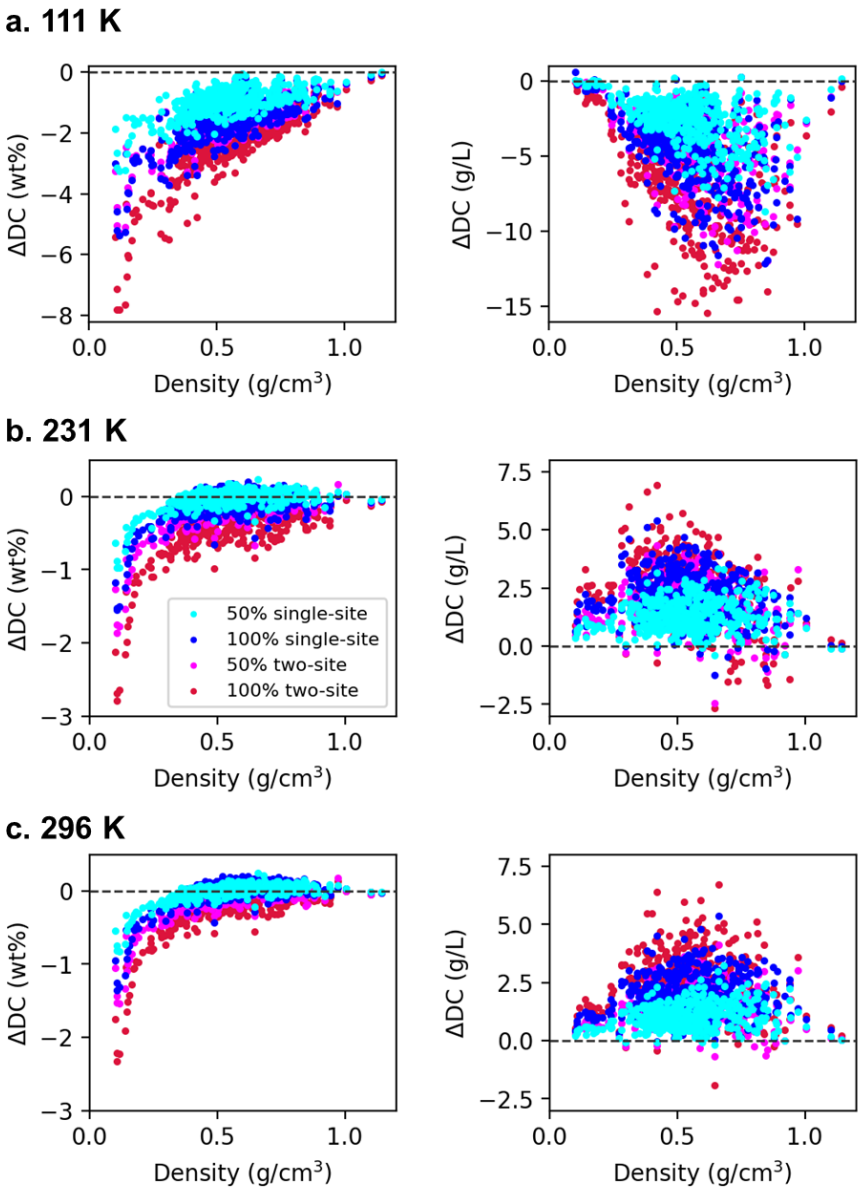

Figure S9. Enhancement of the gravimetric and volumetric H_2 DCs after different types and ratios of functionalization, compared to the density of the original (unfunctionalized) structures. Colors represented the different functionalization, as written in the legend.

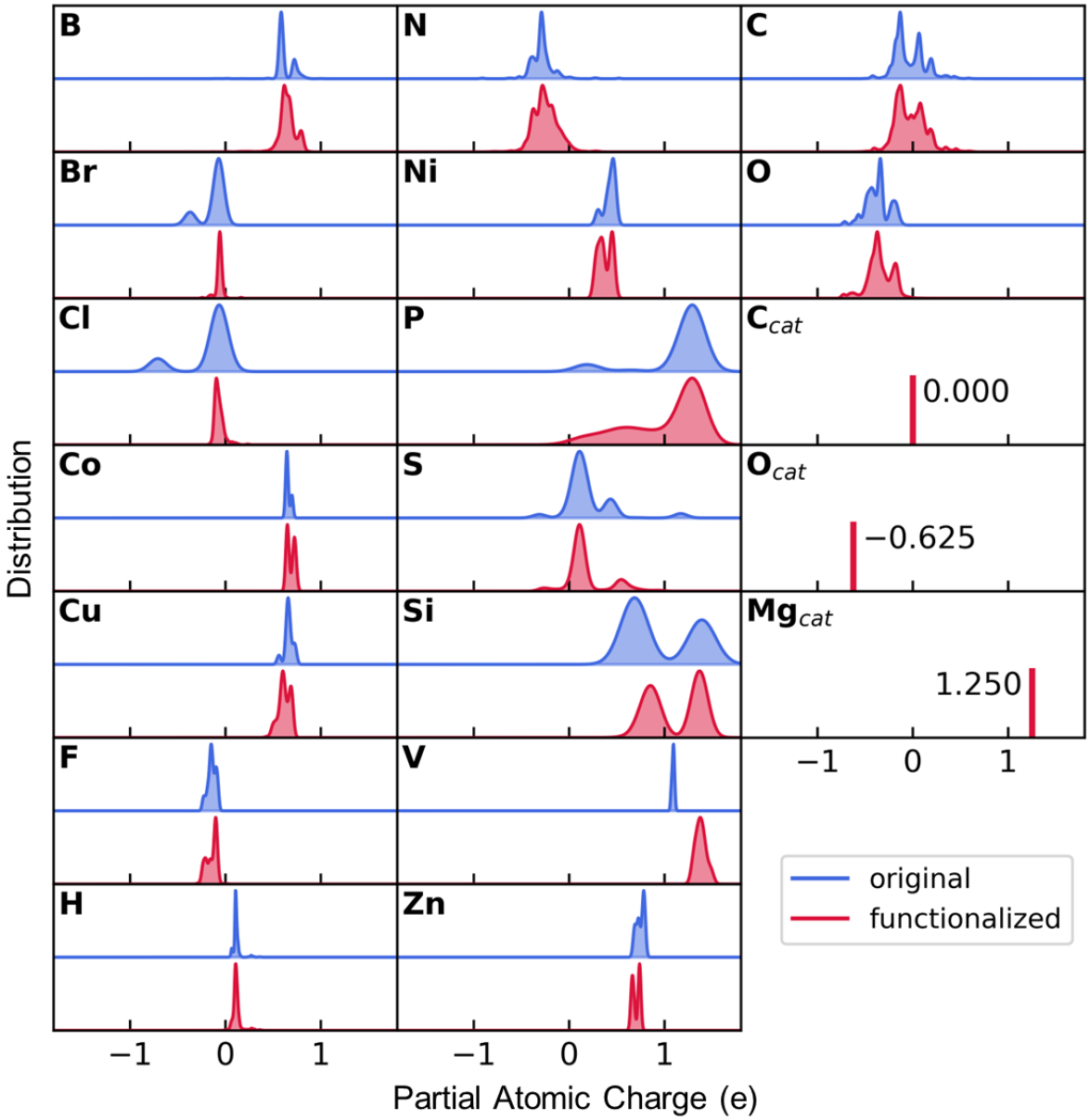

Figure S10. Distribution of partial atomic charges for framework atoms in original unfunctionalized structures (blue) and Mg-alkoxide functionalized structures (red), sorted by element type. For functionalized structures, C_cat, O_cat, and Mg_cat represent the atoms from the functional sites, while C and O without subscripts refer to atoms outside the functional sites.

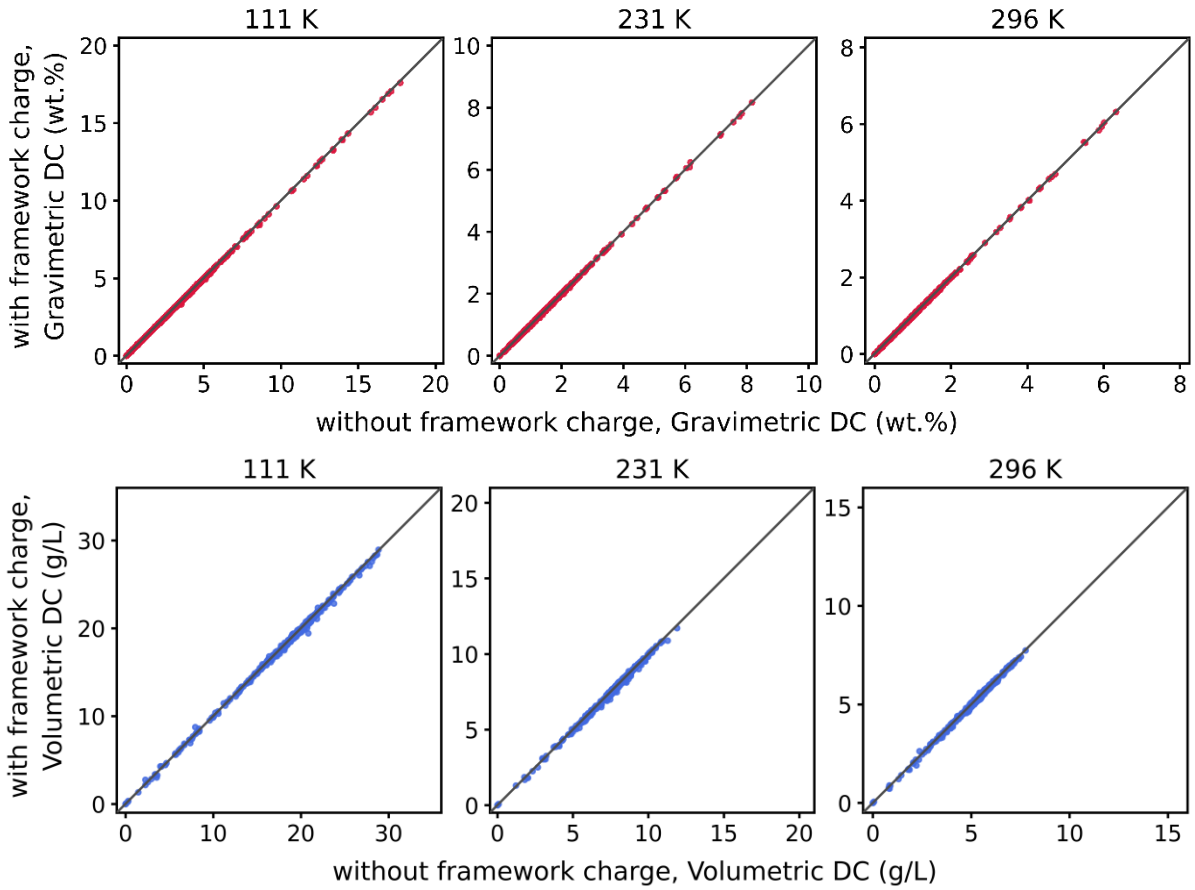

Figure S11. Comparison of the gravimetric (upper) and volumetric (lower) hydrogen DCs of original unfunctionalized structures with framework charges neglected or involved. 609 data points are included in each subplot.

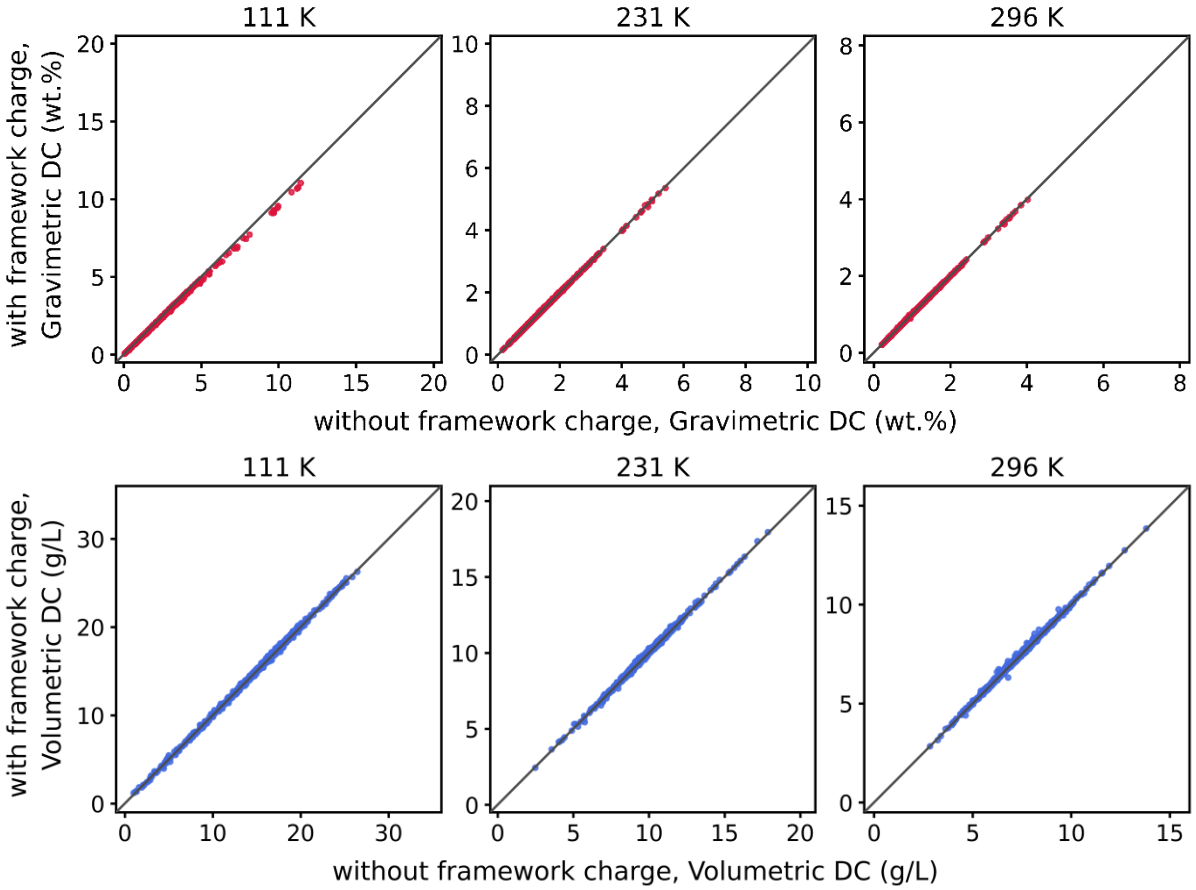

Figure S12. Comparison of the gravimetric (upper) and volumetric (lower) hydrogen DCs of functionalized structures with partial atomic charges assigned only to the Mg and O atoms in the functional sites (without framework charge) or with partial atomic charges assigned to all framework atoms (with framework charge). 905, 929, 936 data points are included in sub-plots of 111 K, 231 K, and 296 K, respectively.

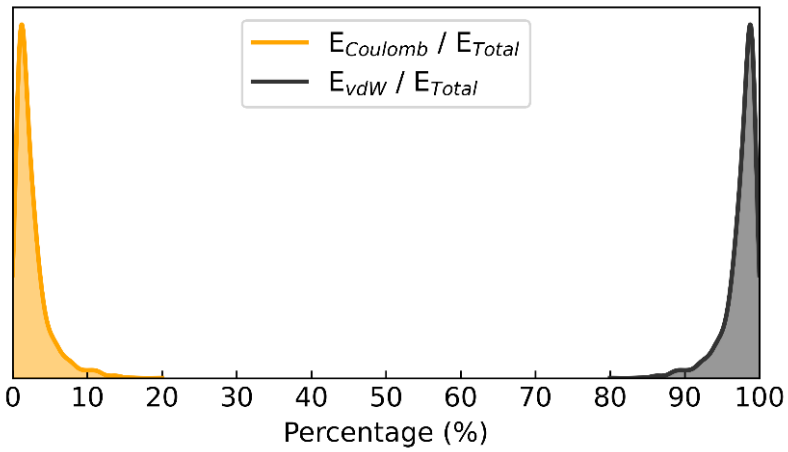

Figure S13. Distribution of the percentages of vdW energies (black) and Coulomb energies (yellow) in the total host-adsorbate energies of all 3,648 GCMC simulations on the 608 original unfunctionalized structures.

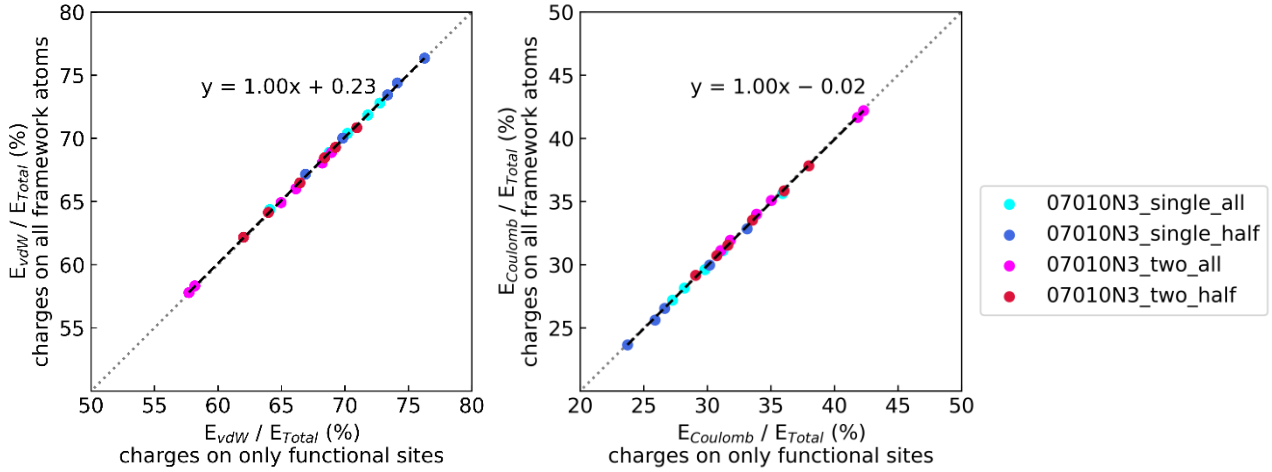

Figure S14. Comparison of the percentages of van der Waals (vdW) energies (left) and Coulomb energies (right) in the total host-adsorbate energies from 22 GCMC simulations on four functionalized 07010N3 structures with different functionalization types and ratios, represented by different colors. The X-axis shows the results with partial atomic charges assigned only to the Mg and O atoms in the functional sites, while the Y-axis shows the results with partial atomic charges assigned to all framework atoms.

S7. Distribution of features and the H_2 adsorption uptakes of COFs in the dataset

Figure S15 shows the distribution of the GCMC-simulated H_2 volumetric uptakes in the dataset. **Figure S16** shows the distribution of the features (textural properties, temperatures, and functionalization types & ratios) and targets (gravimetric and volumetric uptakes) for the ML training.

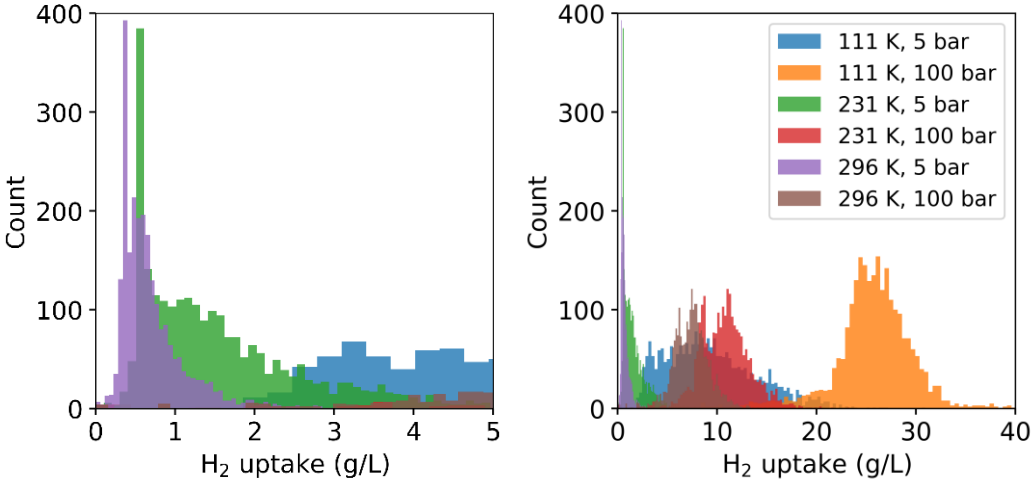

Figure S15. The distribution of the H_2 volumetric uptakes in the dataset. Different colors indicate the uptakes at different T and P conditions, as shown in the legend.

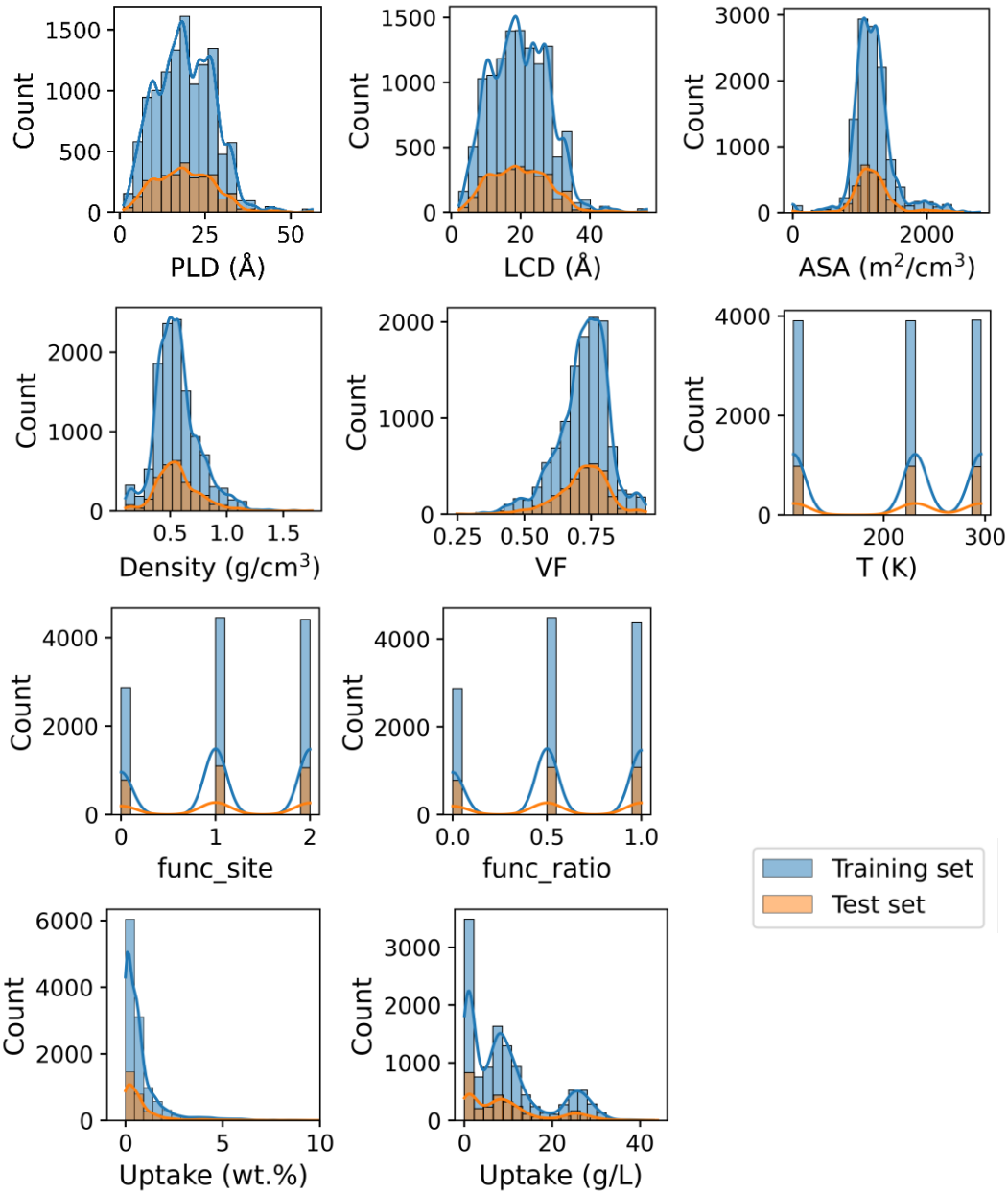

Figure S16. The distribution of the features (textural properties, temperatures, and functionalization types & ratios) and targets (gravimetric and volumetric uptakes) for the ML training.

S8. GCMC simulations of original and functionalized structures with specific FF models of two selected materials

Table S8, Figure S17 and S18 show the H_2 isotherms of the original and functionalized structures of the two selected materials discussed in Section 3.3 in the main text.

The H_2 uptakes of the 100 % two-site functionalized structures, named by _two_all, calculated from the force field developed from single-site model (FF1) and two-site model (FF2) were compared with each other to have a better insight into their description of the adsorptions on the different types of functional sites. As shown in **Figure S17(b)** and **S18(b)**, for the 21320N2_two_all, the H_2 uptakes calculated from FF1 and FF2 did not show significant differences at both lower and ambient temperatures, for both gravimetric and volumetric capacities. This resulted in no difference in the deliverable capacity (DC), defined as the difference between the uptakes at 100 bar and 5 bar. However, for the 07010N3_two_all, the larger number of functionalization sites and different textural properties made the influence of the Mg sites on the overall adsorption behavior more pronounced. The isotherms calculated with FF1 showed a faster increase at low pressure and higher uptakes at high pressure, leading to differences in the DC. At lower temperatures and pressures (e.g., 111 K and 5 bar), the H_2 uptake calculated by FF1 increased faster and showed a larger difference compared to the uptake calculated by FF2. However, at higher pressure near 100 bar, the uptake reached saturation loading, leading to a smaller difference between the uptakes calculated by the different force fields. In summary, FF1 consistently resulted in higher uptakes than FF2. At

low temperatures, the difference between the uptakes calculated by FF1 and FF2 was larger at 5 bar compared to 100 bar, resulting in the DC calculated by FF2 being higher than that calculated by FF1. At ambient temperature, the difference between the uptakes calculated by FF1 and FF2 was smaller at 5 bar compared to 100 bar, leading to the DC calculated by FF2 being lower than that calculated by FF1.

Table S8. Textural properties of the two selected COFs

Structure name	PLD (Å)	LCD (Å)	ASA (m^2/cm^3)	Density (g/cm^3)	VF	# of potential functional sites per unit cell
21320N2	18.1	18.5	1176.11	0.55	0.72	16
07010N3	8.1	9.3	2165.58	0.42	0.77	48

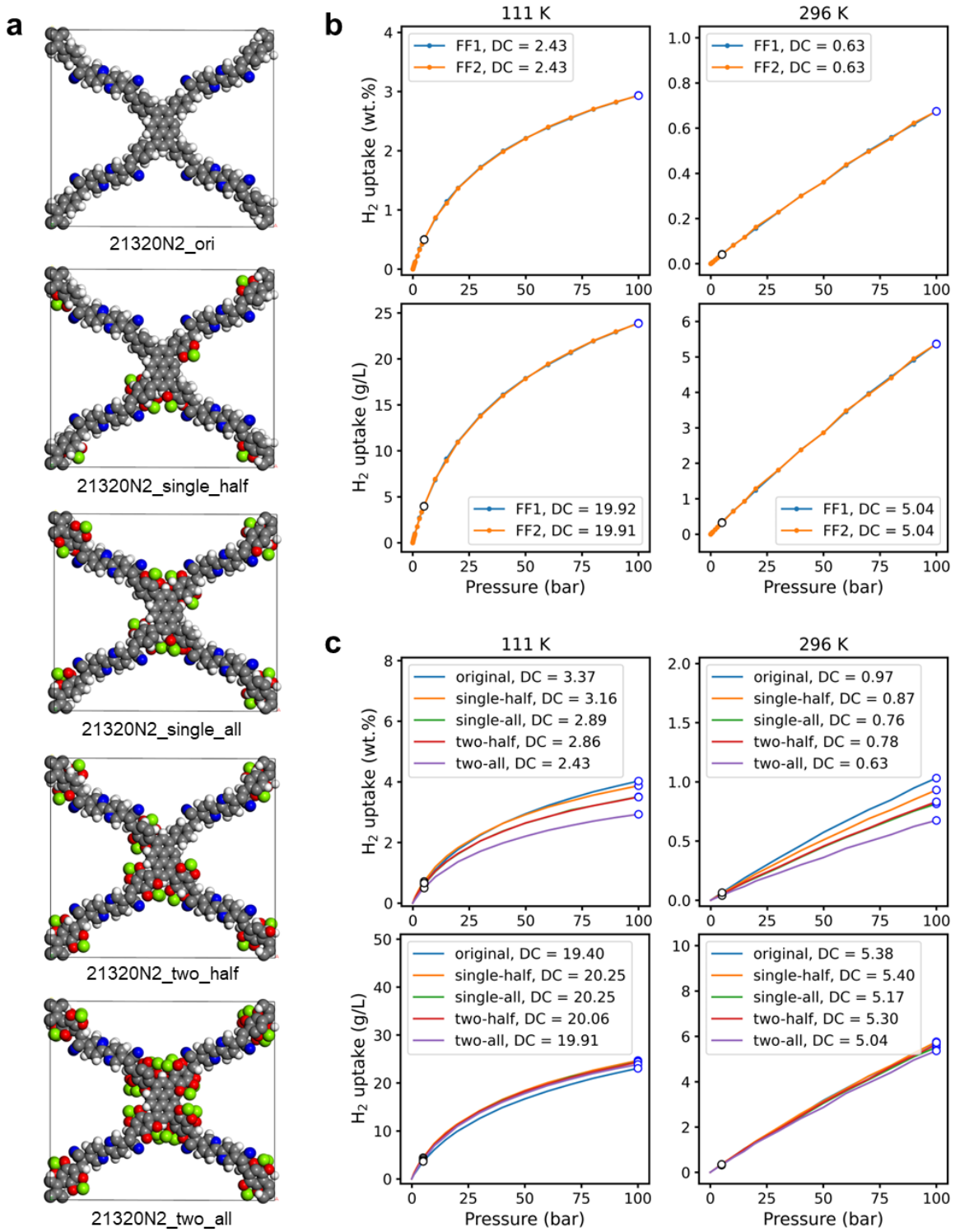

Figure S17. (a) Visualization of original and functionalized structures of 21320N2 (C: grey, N: blue, H: white, O: red, Mg: green). **(b)** H_2 adsorption isotherms of 21320N2_two_all at different temperature, calculated with FF1 and FF2, in gravimetric and volumetric units. **(c)** H_2 adsorption isotherms of original and functionalized 21320N2 at different temperature, calculated with corresponding force fields, in gravimetric and volumetric units.

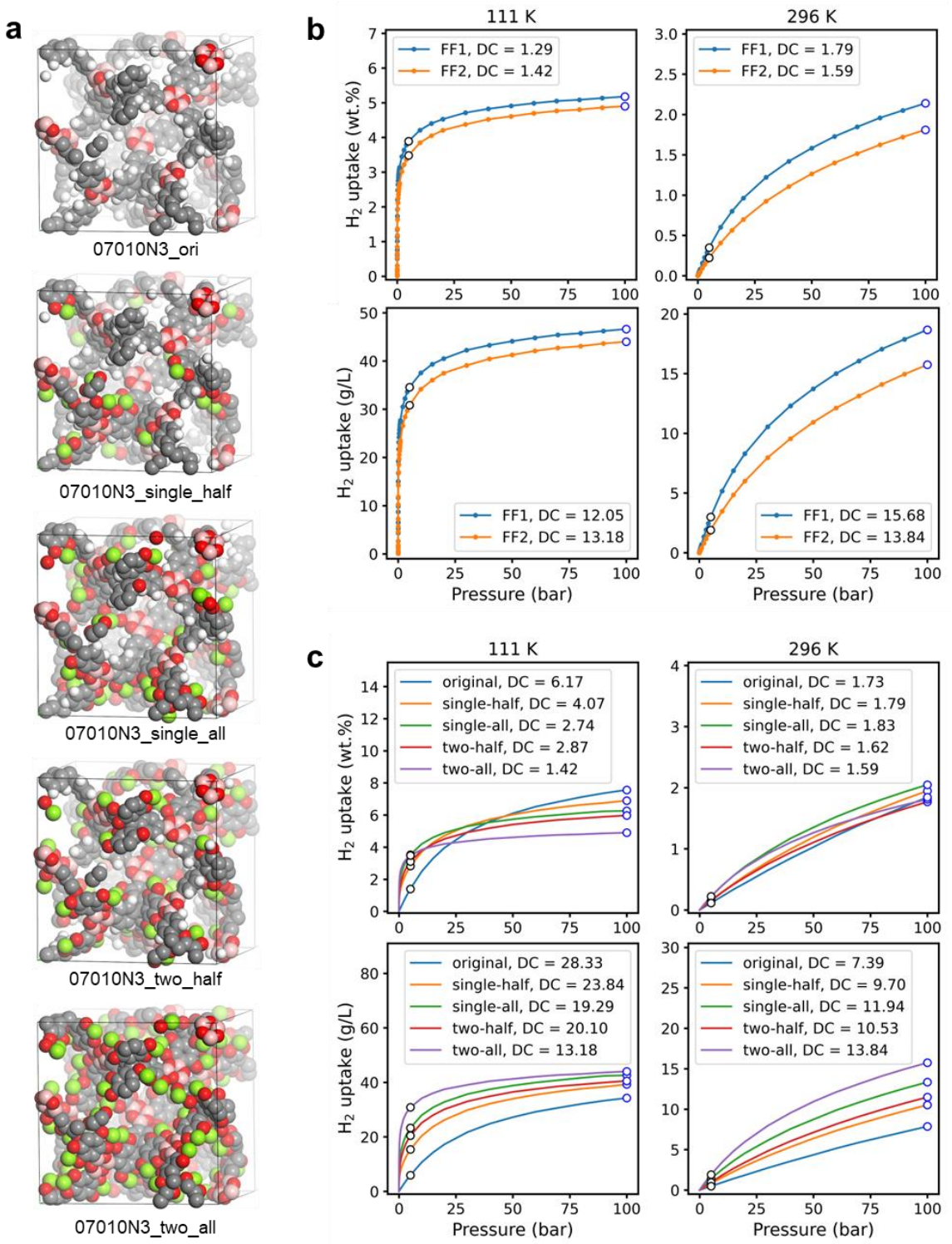

Figure S18. (a) Visualization of original and functionalized structures of 07010N3 (C: grey, N: blue, H: white, O: red, B: pink, Mg: green). **(b)** H_2 adsorption isotherms of 07010N3_two_all at different temperature, calculated with FF1 and FF2, in gravimetric and volumetric units. **(c)** H_2 adsorption isotherms of original and functionalized 07010N3 at different temperature, calculated with corresponding force fields, in gravimetric and volumetric units.

S9. Traditional tree-based ML models training

Three different tree-based ML models, including Gradient Boost Regression (GBR), Random Forest (RF), and Decision Tree Regression (DT), were trained on the same training dataset with the same input features and targets.

Table S9 shows the searching spaces of the hyperparameters of each algorithm. **Table S10** shows the optimal sets of hyperparameter of each trained model. **Table S11** shows the R^2 scores of each trained model. Based on the R^2 scores, the GBR models demonstrate high R^2 scores for both the training and test sets, indicating a lower degree of overfitting. Therefore, the GBR models were considered the best for predicting H_2 uptake among the three algorithms.

Figure S19 shows the comparison between the GBR-predicted and the GCMC-calculated H_2 uptakes of both training and test set, corresponding to the Figure 7(a) in Section 3.4 of the main text. **Figure S20** shows the same comparison, but with coloring the points differently according to the different temperatures.

Table S9. Searching spaces of the hyperparameters of each algorithm

GBR

Hyperparameter	Space
n_estimators	Integer(1,200)
max_depth	Integer(1,10)
num_parallel_tree	Integer(1,10)
min_child_weight	Integer(1,10)
learning_rate	Real(0.001,1)
subsample	Real(0.01,1)
gamma	Real(0.001,10)
alpha	Real(0,1)
reg_alpha	Real(2,10)
reg_lambda	Real(10,5)

RF

Hyperparameter	Space
n_estimators	Integer(1,200)
max_depth	Integer(1,30)
random_state	Integer(1,300)

DT

Hyperparameter	Space
max_depth	Integer(1,30)
min_samples_split	Integer(2,30)
min_samples_leaf	Integer(1,30)

Table S10. The optimal sets of hyperparameter of each trained model

Hyperparameter	GBR_g	GBR_v
n_estimators	183	173
max_depth	6	10
num_parallel_tree	10	10
min_child_weight	5	1
learning_rate	0.4817	1.0
subsample	0.7033	0.4710
gamma	0.001	0.001
alpha	1.0	0.9399
reg_alpha	2.0	2.0
reg_lambda	10.0	14.04

Hyperparameter	RF_g	RF_v
n_estimators	187	200
max_depth	13	21
random_state	300	300

Hyperparameter	DT_g	DT_v
max_depth	9	9
min_samples_split	3	2
min_samples_leaf	1	8

Table S11. R^2 scores of various tree-based ML algorithms for H_2 uptakes prediction.

Algorithm	Target: Gravimetric DC		Target: Volumetric DC	
	Training set	Test set	Training set	Test set
Gradient Boost Regression	0.9977	0.9946	0.9992	0.9939
Random Forest	0.9989	0.9918	0.9835	0.9734
Decision Tree Regression	0.9969	0.9855	0.9979	0.9839

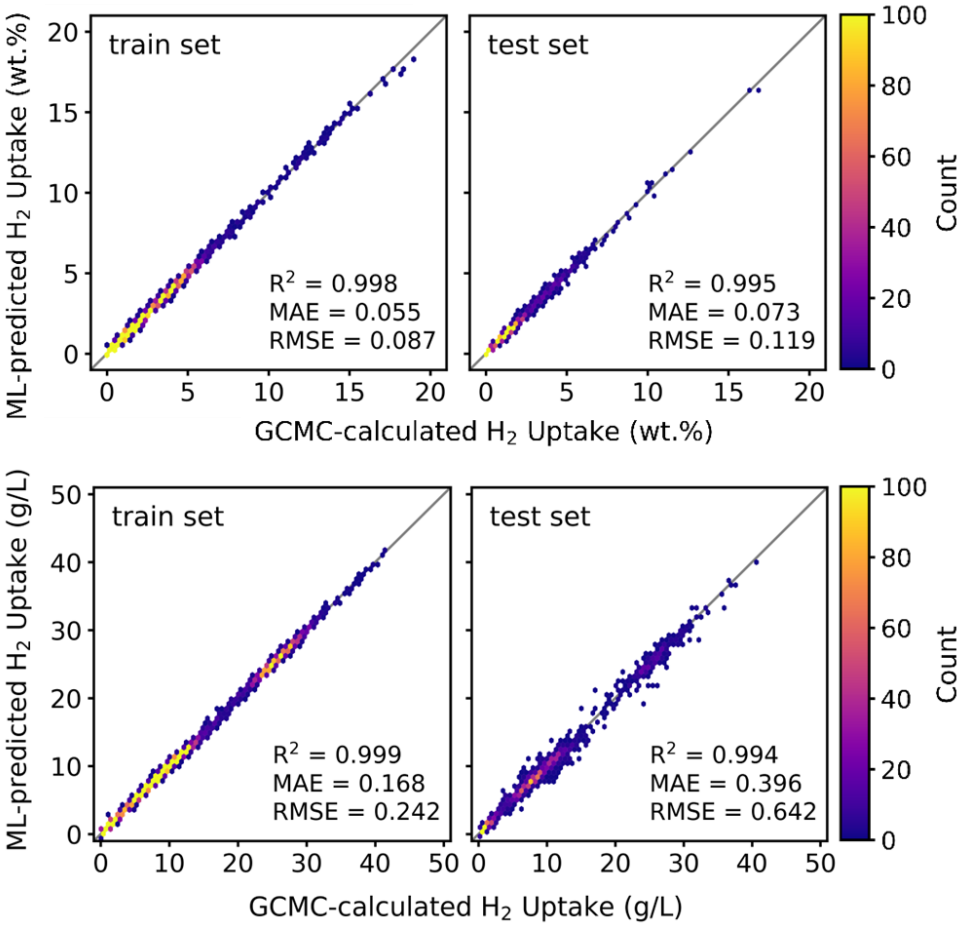

Figure S19. The comparison between the GBR-predicted and the GCMC-calculated H_2 uptakes at both adsorption and desorption pressures of training set (11,731 points) and test set (2,933 points). The upper subplots are the results of GBR_g model predicting the gravimetric uptakes; the lower subplots are the results of GBR_v model predicting the volumetric uptakes.

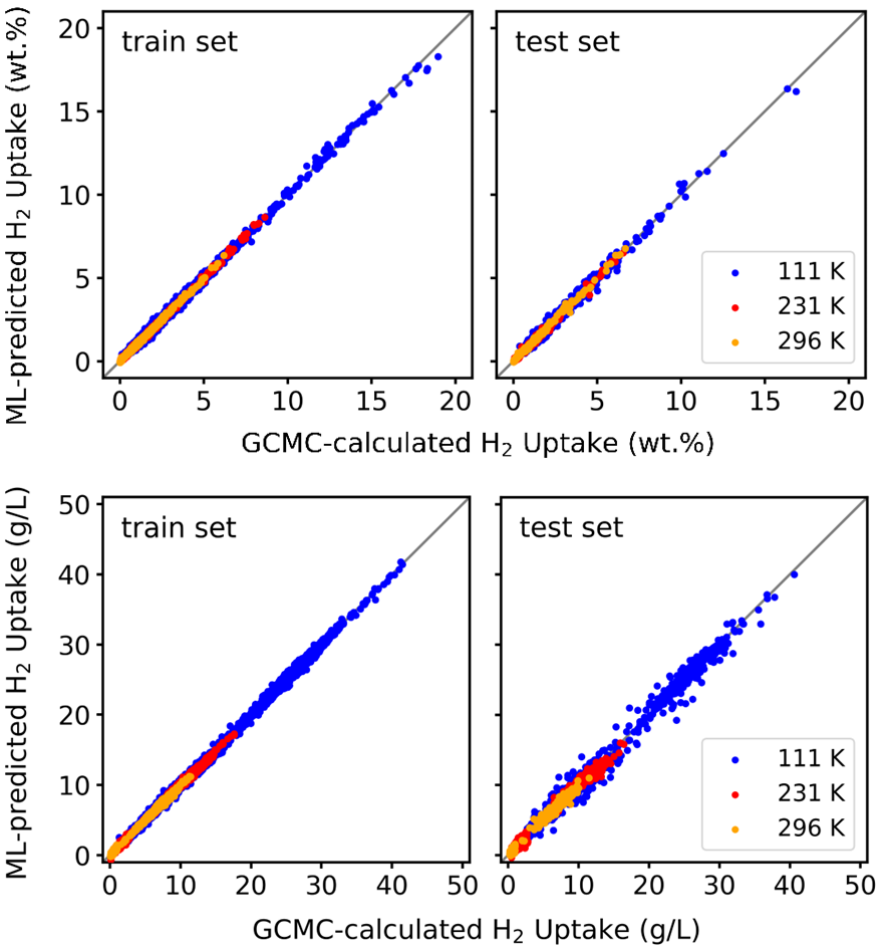

Figure S20. The comparison between the GBR-predicted and the GCMC-calculated H_2 uptakes at both adsorption and desorption pressures, coloring the points differently according to the different temperatures. The upper subplots are the results of GBR_g model predicting the gravimetric uptakes; the lower subplots are the results of GBR_v model predicting the volumetric uptakes.

S10. Crystal Graph Convolutional Neural Network (CGCNN)

An example output list of the CGCNN model was shown in **Table S12**, including 30 values of the uptakes of original/functionalized structures at three different temperatures and two different pressures. The hyperparameters of the CGCNN models were selected manually as shown in **Table S13**. The loss curves of CGCNN_g and CGCNN_v models are showed in **Figure S21**. As shown in the loss curves, the MAE dropped to an acceptable region after 500 epochs and showing no significant evidence of overfitting.

Figure S22 shows the comparison between the CGCNN-predicted and the GCMC-calculated H_2 uptakes of both training and test set, corresponding to the Figure 9(a) in Section 3.4 of the main text. **Figure S23** shows the same comparison, but with coloring the points differently according to the different temperatures.

Table S12. Example output list of the CGCNN models

ori_111_5	ori_111_100	ori_231_5	ori_231_100	ori_296_5	ori_296_100
4.25	25.82	0.60	8.99	0.39	6.27
single_half_111_5	**single_half_111_100**	**single_half_231_5**	**single_half_231_100**	**single_half_296_5**	**single_half_296_100**
8.96	29.04	1.01	11.12	0.51	7.42
single_all_111_5	**single_all_111_100**	**single_all_231_5**	**single_all_231_100**	**single_all_296_5**	**single_all_296_100**
11.40	27.90	1.62	12.00	0.67	8.14
two_half_111_5	**two_half_111_100**	**two_half_231_5**	**two_half_231_100**	**two_half_296_5**	**two_half_296_100**
9.69	28.16	0.93	10.97	0.49	7.30
two_all_111_5	**two_all_111_100**	**two_all_231_5**	**two_all_231_100**	**two_all_296_5**	**two_all_296_100**
15.79	30.74	1.94	13.51	0.75	8.88

Table S13. The hyperparameter of the trained CGCNN models

Hyperparameter	Search space	Final adopted
Epoch	500, 1000	500
Optimizer	SGD	SGD
Learning rate	0.001, 0.05, 0.01	0.001
Momentum	0.9	0.9
weight_decay	1e-6	1e-6
Batch size	4	4
# of convolutional layers	3, 5	3
# of hidden layers	1, 3	1
Activate function	Softplus	Softplus

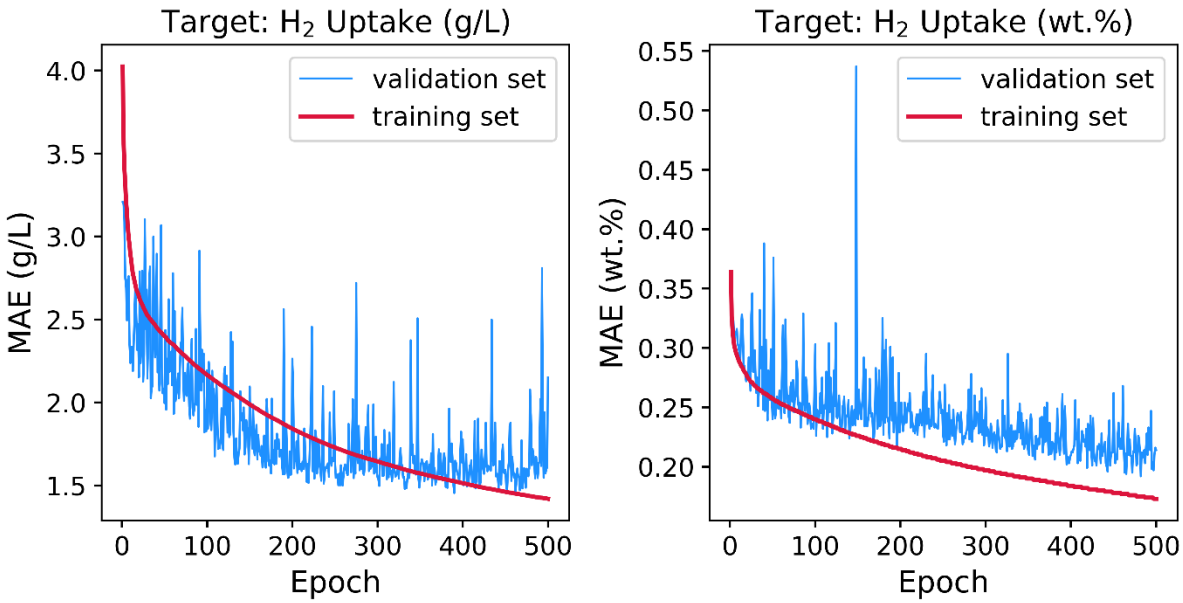

Figure S21. The loss curves of final-adopted CGCNN_v and CGCNN_g models.

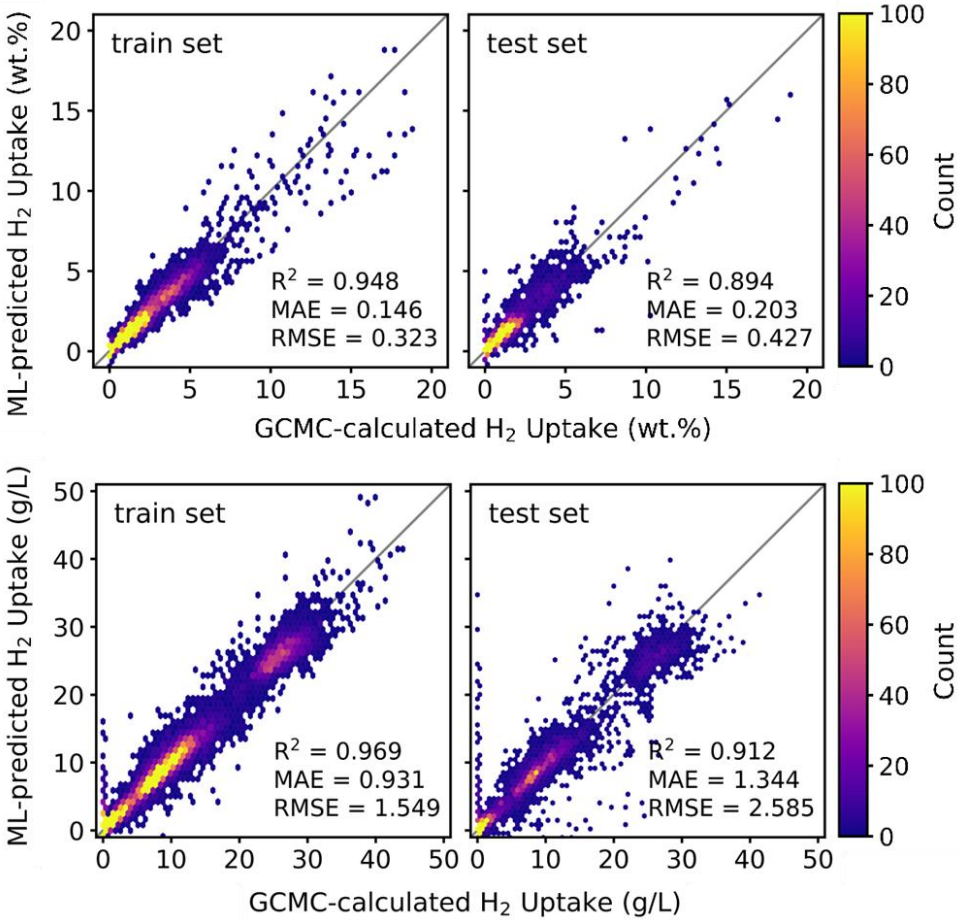

Figure S22. The comparison between the CGCNN-predicted and the GCMC-calculated H_2 uptakes at both adsorption and desorption pressures and of training set (14,190 points) and test set (3,540 points). The upper subplots are the results of CGCNN_g model predicting the gravimetric uptakes; the lower subplots are the results of CGCNN_v model predicting the volumetric uptakes.

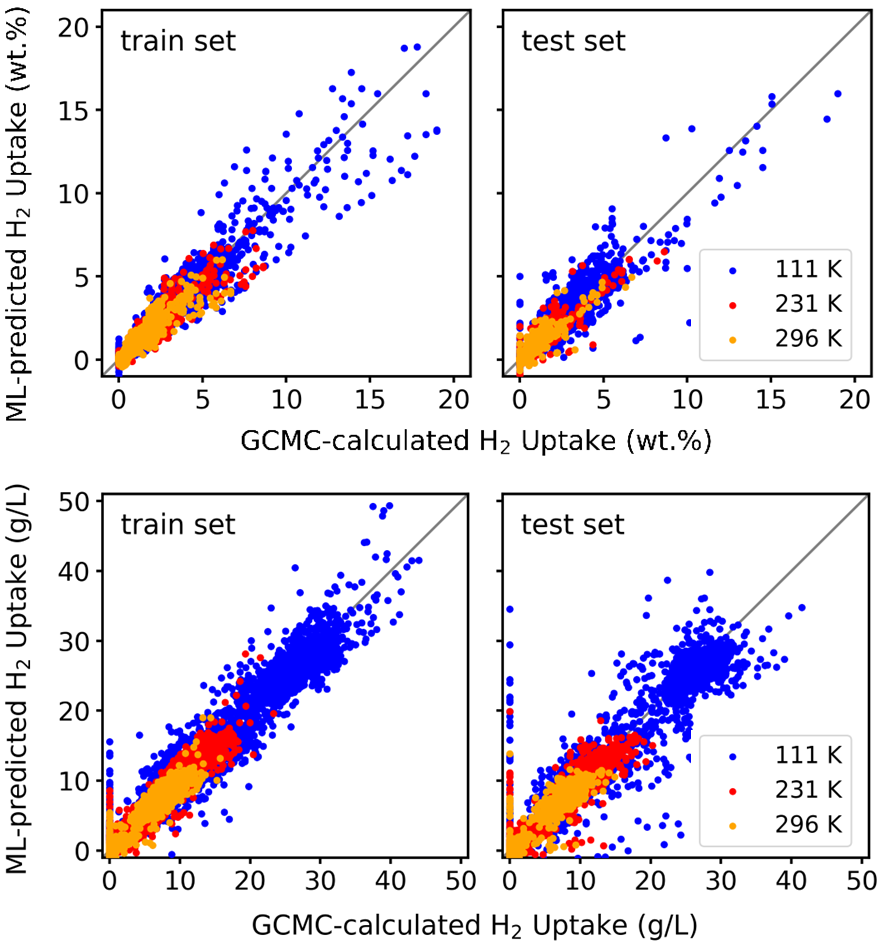

Figure S23. The comparison between the CGCNN-predicted and the GCMC-calculated H_2 uptakes at both adsorption and desorption pressures, coloring the points differently according to the different temperatures. The upper subplots are the results of CGCNN_g model predicting the gravimetric uptakes; the lower subplots are the results of CGCNN_v model predicting the volumetric uptakes.

S11. ML prediction of H_2 storage capacity of hypothetical COF structures in ReDD-COFFEE database (DB)

With the help of our trained GBR models, we are now able to efficiently screen hypothetical COFs from the ReDD-COFFEE DB. It is important that the textural properties of two datasets (CURATED-COF DB that ML model is trained on and ReDD-COFFEE DB that developed ML model was used to predict H_2 properties). The textural property data for the COFs in the ReDD-COFFEE DB, such as accessible surface area and pore volume, were calculated using a probe radius of 1.84 Å, which is consistent with the dataset our GBR model is trained on.

Figure S24 compares the textural properties of the CURATED-COF DB cover most of those from the ReDD-COFFEE DB. However, as illustrated by the distribution curves, the hypothetical COFs from ReDD-COFFEE tend to have lower density and larger void fraction (VF), which significantly differs from the distribution observed in CURATED-COFs. Since both VF and density are key factors in predicting adsorption performance, this disparity could introduce some inaccuracies in the predictions when applying the GBR models trained on CURATED-COFs to the ReDD-COFFEE database.

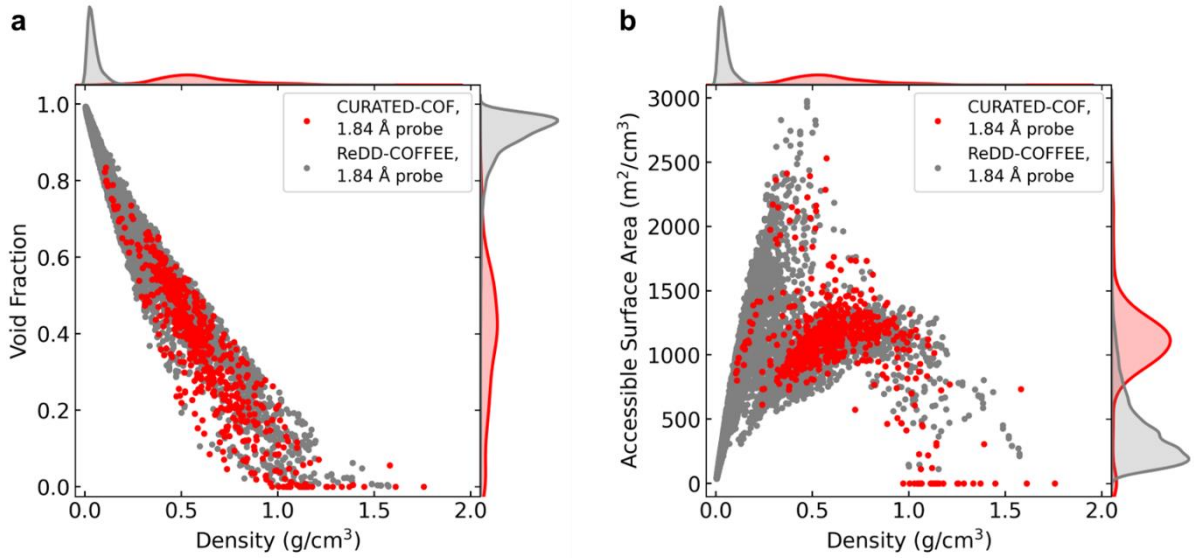

Figure S24. Comparison of the textural properties of different database calculated with different probe radius. The kernel density estimation (KDE) curves on the x and y axis represent the distribution of each property. **(a)** Density vs. VF, with the 1.84 Å probe radius; **(b)** Density vs. ASA, with the 1.84 Å probe radius.

REFERENCE

(1) Anderson, G.; Schweitzer, B.; Anderson, R.; Gómez-Gualdrón, D. A. Attainable Volumetric Targets for Adsorption-Based Hydrogen Storage in Porous Crystals: Molecular Simulation and Machine Learning. *The Journal of Physical Chemistry C* **2019**, *123* (1), 120-130.
(2) Desgranges, C.; Delhommelle, J. Ensemble Learning of Partition Functions for the Prediction of Thermodynamic Properties of Adsorption in Metal–Organic and Covalent Organic Frameworks. *The Journal of Physical Chemistry C* **2020**, *124* (3), 1907-1917.
(3) Aksu, G. O.; Keskin, S. Advancing CH 4/H 2 separation with covalent organic frameworks by combining molecular simulations and machine learning. *J. Mater. Chem. A* **2023**, *11* (27), 14788-14799.
(4) Tsivion, E.; Long, J. R.; Head-Gordon, M. Hydrogen Physisorption on Metal–Organic Framework Linkers and Metalated Linkers: A Computational Study of the Factors That Control Binding Strength. *J. Am. Chem. Soc.* **2014**, *136* (51), 17827-17835.
(5) Veccham, S. P.; Head-Gordon, M. Density Functionals for Hydrogen Storage: Defining the H2Bind275 Test Set with Ab Initio Benchmarks and Assessment of 55 Functionals. *J. Chem. Theory Comput.* **2020**, *16* (8), 4963-4982.
(6) Chakraborty, R.; Talbot, J. J.; Shen, H.; Yabuuchi, Y.; Carsch, K. M.; Jiang, H. Z. H.; Furukawa, H.; Long, J. R.; Head-Gordon, M. Quantum chemical modeling of hydrogen binding in metal–organic frameworks: validation, insight, predictions and challenges. *Physical Chemistry Chemical Physics* **2024**, *26* (8), 6490-6511.
(7) Xiang, Y.; Sun, D. Y.; Fan, W.; Gong, X. G. Generalized simulated annealing algorithm and its application to the Thomson model. *Physics Letters A* **1997**, *233* (3), 216-220.
(8) Tsallis, C. Possible generalization of Boltzmann-Gibbs statistics. *Journal of Statistical Physics* **1988**, *52* (1), 479-487.
(9) Tsallis, C.; Stariolo, D. A. Generalized simulated annealing. *Physica A: Statistical Mechanics and its Applications* **1996**, *233* (1), 395-406.
(10) Xiang, Y.; Gong, X. Efficiency of generalized simulated annealing. *Physical Review E* **2000**, *62* (3), 4473.
(11) Zhao, G.; Chung, Y. G. PACMAN: A Robust Partial Atomic Charge Predicter for Nanoporous Materials Based on Crystal Graph Convolution Networks. *Journal of Chemical Theory and Computation* **2024**, *20* (12), 5368-5380.